

This work was written as part of one of the author's official duties as an Employee of the United States Government and is therefore a work of the United States Government. In accordance with 17 U.S.C. 105, no copyright protection is available for such works under U.S. Law. Access to this work was provided by the University of Maryland, Baltimore County (UMBC) ScholarWorks@UMBC digital repository on the Maryland Shared Open Access (MD-SOAR) platform.

Please provide feedback

Please support the ScholarWorks@UMBC repository by emailing scholarworks-group@umbc.edu and telling us what having access to this work means to you and why it's important to you. Thank you.



An analysis of fast photochemistry over high northern latitudes during spring and summer using in-situ observations from ARCTAS and TOPSE

J. R. Olson¹, J. H. Crawford¹, W. Brune², J. Mao³, X. Ren⁴, A. Fried^{5,*}, B. Anderson¹, E. Apel⁵, M. Beaver^{6,**}, D. Blake⁷, G. Chen¹, J. Crounse⁶, J. Dibb⁸, G. Diskin¹, S. R. Hall⁵, L. G. Huey⁹, D. Knapp⁵, D. Richter⁵, D. Rierner¹⁰, J. St. Clair⁶, K. Ullmann⁵, J. Walega⁵, P. Weibring⁵, A. Weinheimer⁵, P. Wennberg⁶, and A. Wisthaler^{11,***}

¹NASA Langley Research Center, Hampton, VA, USA

²Department of Meteorology, Penn State, University Park, PA, USA

³Atmospheric and Oceanic Sciences, Department of Geosciences, Princeton University, Princeton, NJ, USA

⁴NOAA Air Resources Laboratory, Silver Spring, MD, USA

⁵NCAR, Boulder, CO, USA

⁶California Institute of Technology, Pasadena, CA, USA

⁷School of Physical Sciences, Department of Chemistry, University of California, Irvine, CA, USA

⁸School of Physical Sciences, Department of Chemistry, University of New Hampshire, Durham, NH, USA

⁹Georgia Institute of Technology, Atlanta, GA, USA

¹⁰Rosenstiel School of Marine and Atmospheric Science, University of Miami, Miami, FL, USA

¹¹Institute for Ion Physics and Applied Physics, University of Innsbruck, Innsbruck, Austria

* now at: Institute of Arctic and Alpine Research, University of Colorado, Boulder, CO, USA

** now at: Environmental Protection Agency, Research Triangle Park, NC, USA

*** now at: Norwegian Institute of Air Research, Kjeller, Norway

Correspondence to: J. R. Olson (jennifer.r.olson@nasa.gov)

Received: 12 March 2012 – Published in Atmos. Chem. Phys. Discuss.: 11 April 2012

Revised: 9 July 2012 – Accepted: 10 July 2012 – Published: 1 August 2012

Abstract. Observations of chemical constituents and meteorological quantities obtained during the two Arctic phases of the airborne campaign ARCTAS (Arctic Research of the Composition of the Troposphere from Aircraft and Satellites) are analyzed using an observationally constrained steady state box model. Measurements of OH and HO₂ from the Penn State ATHOS instrument are compared to model predictions. Forty percent of OH measurements below 2 km are at the limit of detection during the spring phase (ARCTAS-A). While the median observed-to-calculated ratio is near one, both the scatter of observations and the model uncertainty for OH are at the magnitude of ambient values. During the summer phase (ARCTAS-B), model predictions of OH are biased low relative to observations and demonstrate a high sensitivity to the level of uncertainty in NO observations. Predictions of HO₂ using observed CH₂O and H₂O₂

as model constraints are up to a factor of two larger than observed. A temperature-dependent terminal loss rate of HO₂ to aerosol recently proposed in the literature is shown to be insufficient to reconcile these differences. A comparison of ARCTAS-A to the high latitude springtime portion of the 2000 TOPSE campaign (Tropospheric Ozone Production about the Spring Equinox) shows similar meteorological and chemical environments with the exception of peroxides; observations of H₂O₂ during ARCTAS-A were 2.5 to 3 times larger than those during TOPSE. The cause of this difference in peroxides remains unresolved and has important implications for the Arctic HO_x budget. Unconstrained model predictions for both phases indicate photochemistry alone is unable to simultaneously sustain observed levels of CH₂O and H₂O₂; however when the model is constrained with observed CH₂O, H₂O₂ predictions from a range of

rainout parameterizations bracket its observations. A mechanism suitable to explain observed concentrations of CH_2O is uncertain. Free tropospheric observations of acetaldehyde (CH_3CHO) are 2–3 times larger than its predictions, though constraint of the model to those observations is sufficient to account for less than half of the deficit in predicted CH_2O . The box model calculates gross O_3 formation during spring to maximize from 1–4 km at 0.8 ppbv d^{-1} , in agreement with estimates from TOPSE, and a gross production of 2–4 ppbv d^{-1} in the boundary layer and upper troposphere during summer. Use of the lower observed levels of HO_2 in place of model predictions decreases the gross production by 25–50 %. Net O_3 production is near zero throughout the ARCTAS-A troposphere, and is 1–2 ppbv in the boundary layer and upper altitudes during ARCTAS-B.

1 Introduction

The climate of the Arctic environment is changing more rapidly than any other region. While polar temperature trends vary, the overall trend is one of substantial warming (Arctic Climate Impact Assessment <http://amap.no/acia/>), and the September sea ice extent is decreasing at accelerating rates (Lemke et al., 2007; Comiso et al., 2008). Studies indicate that regional radiative forcing from aerosols and tropospheric O_3 is likely to be a significant contributor to the Arctic warming trend during the winter and spring, and that factors controlling these constituents in the Arctic are poorly understood and simulated (Stohl, 2006; Law and Stohl, 2007; Shindell et al., 2007; Quinn et al., 2008).

A major mechanism for long-range transport of O_3 , aerosols and other pollutants into high latitudes is the near-surface transport of pollution from northern Euro-Asian sources into the wintertime Arctic (the “Arctic haze” phenomenon; e.g., Radke et al., 1984; Brock et al., 1989; Shaw, 1995). Recent studies have expanded upon that understanding to show that transport of middle latitude pollutants into the Arctic can occur throughout the extent of the Arctic troposphere at various times throughout the year, from source regions located in Asia, Europe and North America (Stohl, 2006; Shindell et al., 2008; Singh et al., 2010; Fisher et al., 2010). Additionally, emissions from high latitude boreal forest fires over North America and Asia are transported into the Arctic predominantly during summer, but evidence of long range transport from fires is found during spring as well (Scheuer et al., 2003; Singh et al., 2010).

O_3 photochemistry at high latitudes is impacted by several unique characteristics: extreme cold and dry conditions and long seasonal periods of darkness followed by long periods of sunlight at high solar zenith angles. The persistent snow and sea ice surface increases incident radiation due to a heightened surface albedo, and photochemical reactions within the snowpack itself result in emissions of gases

such as hydrogen peroxide (H_2O_2), formaldehyde (CH_2O), and HONO, which can impact near-surface HO_x chemistry (Chen et al., 2004; Frey et al., 2009). During spring, enhanced concentrations of gaseous bromine radicals (BrO) are frequently observed over Arctic sea ice upon polar sunrise. The catalytic cycling of these halogen radicals has been implicated as the cause of local scale near-complete destruction of surface O_3 and further, they influence the cycling and photochemistry of HO_x , NO_x , and O_3 . (e.g., Barrie et al., 1988; Evans et al., 2003; McElroy et al., 1999; von Glasow et al., 2004). Studies stemming from the 2000 TOPSE aircraft campaign (Tropospheric Ozone Production about the Spring Equinox) highlight the importance of photochemistry at high latitudes, suggesting that gross photochemical O_3 formation is equal to or greater than the source from long range transport throughout the spring in the free troposphere, and is greater than transport sources at surface altitudes after March (Stroud et al., 2004; Emmons et al., 2003).

This study examines fast photochemistry from the perspective of in-situ data and model analysis during the high latitude spring and summer, including radical budgets and cycling, and O_3 production and destruction. The data are from NASA’s 2008 ARCTAS (Arctic Research of the Composition of the Troposphere from Aircraft and Satellites) campaign, and data from springtime high latitudes from portions of the TOPSE campaign are compared to ARCTAS.

2 Data and modeling approach

2.1 Campaign deployments

2.1.1 ARCTAS

The high-latitude portion of ARCTAS was comprised of two deployment phases during spring and summer of 2008 and utilized three aircraft: the NASA DC-8, P-3B and B-200. The DC-8 instrumentation provided a suite of measurements of species related to aerosol and tropospheric O_3 chemistry, pollution sources, and radical chemistry. A more complete description of the aircraft payload is in Jacob et al. (2010).

The spring deployment phase (ARCTAS-A) was based out of Fairbanks, Alaska (65° N , 148° W) from 1–19 April, during which the DC-8 flew 9 sorties across the Arctic between Alaska, Thule Greenland, and Iqaluit Canada (see Fig. 1 for DC-8 flight paths during ARCTAS). The summer phase (ARCTAS-B) was based out of Cold Lake, Edmonton Canada (54° N , 110° W) from 26 June–14 July, with 9 sorties ranging across Canada and up to Thule and Summit in Greenland. A third phase (ARCTAS-CARB) took place immediately prior to ARCTAS-B in coordination with the California Air Resources Board (CARB), and was focused on middle latitude pollution off the coast of California to improve state emission inventories for greenhouse gases and

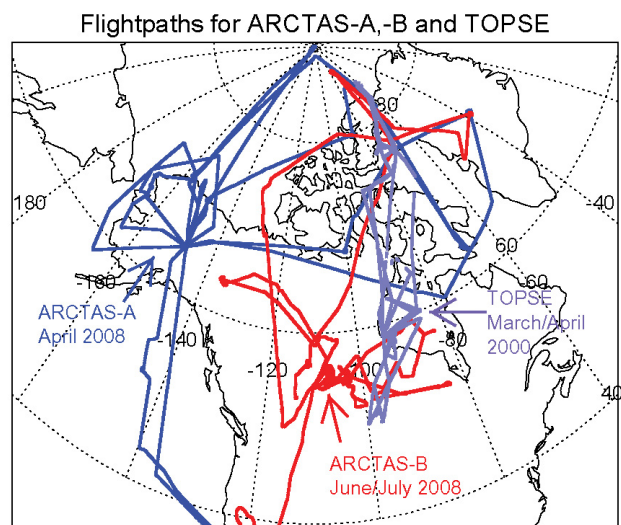


Fig. 1. Flight paths for the NASA DC-8 during ARCTAS-A and -B, and for the NCAR C-130 during TOPSE-sp (subset of TOPSE data obtained during March and April and north of 50° N).

aerosols. The weight of analysis for this high latitude study is on ARCTAS-A and -B.

2.1.2 TOPSE

During 2000, NCAR (National Center for Atmospheric Research) sponsored the airborne experiment TOPSE (Tropospheric Ozone Production about the Spring Equinox); it was conducted using an instrumented C-130 aircraft from February–May 2000, which brackets the seasonal period covered by ARCTAS-A. The geographical extent of the campaign included middle and high latitudes over North America (40–85° N) (Atlas et al., 2003). The high latitude data covered a relatively narrow longitude range over central to eastern Canada and up to Thule, Greenland, meaning most data was obtained further to the east over the North American high latitudes and nearly a decade earlier than during ARCTAS-A (see Fig. 1). Nevertheless, it is reasonable to compare data obtained within the high latitude air masses during these two campaigns. Here, the subset of the TOPSE data obtained during March and April at latitudes north of 50° N is considered (herein called TOPSE-sp).

2.2 Box model

The NASA Langley Research Center photochemical box model (LaRC-V08) (Crawford et al., 1999; Olson et al., 2006) uses a diurnal steady state (DSS) approach with long-lived species constrained to measurements. In the DSS approach, each input point of in-situ data (generally taken from data merges averaged to a 1-min common timeline) is integrated by the model to find an internally self-consistent diurnal cycle for all computed species to within a given toler-

ance (< 1 %). Predictions are then taken from the computed diurnal cycle at the same time of day as the data for direct comparison of radical predictions and measurements. Reactions and rates for basic HO_x - NO_x - CH_4 - CO chemistry are those recommended by Sander et al. (2006) and Atkinson et al. (2006). Non-methane hydrocarbon (NMHC) chemistry is originally based on the lumped scheme from Lurmann et al. (1986), with adjustments as discussed in the appendix of Crawford et al. (1999). Because halogen chemistry is expected to impact surface O_3 chemistry and radical cycling near the surface and in the lower troposphere the box model is updated to include bromine photochemistry (see Table 1).

As in previous studies, photolysis rate coefficients are based on in-situ measurements (Shetter and Muller, 1999). A DISORT four-stream implementation of the NCAR Tropospheric Ultraviolet Visible (TUV) radiative transfer code is first used to calculate the diurnal variation of photolysis rates for clear-sky conditions (Madronich and Flocke, 1998). To adjust these clear-sky rates to account for local cloudiness and surface reflectance, a normalization factor is applied so that observed rates at the time of observation are matched. In the event that a given radical precursor is not constrained to observations, surface deposition and rain-out for soluble species are parameterized as in Logan et al. (1981), i.e., for altitudes < 1 km, a surface deposition loss rate of $1 \times 10^{-5} \text{ s}^{-1}$ is assigned to most species impacted by surface deposition, with a smaller loss rate of $0.3 \times 10^{-5} \text{ s}^{-1}$ for CH_3OOH . Above the boundary layer, the rainout parameterization assumes a 5 day lifetime for altitudes up to 4 km, with an exponentially decreasing loss rate above. Aerosol and cloud uptake for HO_2 is not directly computed in the base simulation but potential impacts of heterogeneous loss in the high latitude environment (e.g., Mao et al., 2010) are explored.

Model calculations require constraint to observations of temperature, pressure, H_2O , O_3 , CO , NO , CH_4 , NMHCs, ketones (acetone and MEK), and alcohols (methanol and ethanol). In addition to these minimum requirements, several additional constraints may be incorporated if desired when measurements are available; these include CH_2O , H_2O_2 and CH_3OOH , nitric acid (HNO_3), peroxy acetyl nitrate (PAN), and BrO . Constraining parameters are held constant throughout the diurnal cycle with the exception of NO . The total short-lived nitrogen ($\text{NO} + \text{NO}_2 + \text{NO}_3 + 2\text{N}_2\text{O}_5 + \text{HONO} + \text{HNO}_4$) is held constant, with partitioning into the individual species calculated by the model throughout the day. The sum total of short-lived nitrogen is determined when NO matches the observed value at the time of measurement.

There are occasions when pronounced heterogeneity of 1 Hz NO measurements within the averaged 1 min time span can result in erroneous model predictions of HO_x and related radical species (Olson et al., 2006). In these cases, the 1 min average has been broken into 60 one-second points for modeling purposes, using 1 Hz data for NO , O_3 , CO and H_2O . The high-resolution model predictions are then

Table 1. Bromine reactions included in the model.

Reaction	Rate Coefficient, cm ³ molec ⁻¹ s ⁻¹	Reference	Reaction Number
Br+O ₃ →BrO+O ₂	$1.7 \times 10^{-11} e^{(-800/T)}$	Sander et al. (2006)	(R1)
Br+CH ₂ O→HBr+HO ₂	$7.7 \times 10^{-12} e^{(-580/T)}$	Atkinson et al. (2006)	(R2)
Br+CH ₃ CHO→HBr+MCO ₃	$1.8 \times 10^{-11} e^{(-460/T)}$	Atkinson et al. (2006)	(R3)
Br+ALD ₃ →HBr+RCO ₃	$5.75 \times 10^{-11} e^{(-610/T)}$	Atkinson et al. (2006)	(R4)
Br+HO ₂ →HBr+O ₂	$4.8 \times 10^{-12} e^{(-310/T)}$	Sander et al. (2006)	(R5)
Br+BrONO ₂ →Br ₂ +NO ₃	$1.78 \times 10^{-11} e^{(-365/T)}$	NIST,Soller et al. (2001)	(R6)
Br+C ₂ H ₂ →HBr+HO ₂ +2CO	$6.35 \times 10^{-15} e^{(440/T)}$	Atkinson et al. (2006)	(R7)
Br+C ₂ H ₄ →BrMCO ₃ +Products	$2.8 \times 10^{-13} e^{(224/T)} \frac{B}{B+8.5 \times 10^{12} e^{(-3200/T)}}$ where $B = 7.5 \times 10^{-12} [O_2]$	Atkinson et al. (2006)	(R8)
HBr+OH→Br+H ₂ O	$5.5 \times 10^{-12} e^{(200/T)}$	Sander et al. (2006)	(R9)
BrO+HO→ ₂ HOBr+O ₂	$4.5 \times 10^{-12} e^{(460/T)}$	Sander et al. (2006)	(R10)
BrO+CH ₃ O ₂ → .25(CH ₂ O+HO ₂ +O ₃)+ .75(HOBr+CH ₂ O ₂)	5.7×10^{-12}	Atkinson et al. (2006)	(R11)
BrO+NO→Br+NO ₂	$8.8 \times 10^{-12} e^{(260/T)}$	Atkinson et al. (2006)	(R12)
BrO+NO ₂ (+M)→BrONO ₂	$\left(\frac{K_0[M]}{1+\frac{K_0[M]}{K_\infty}} \right) 0.6 \left\{ 1 + \left[\log_{10} \left(\frac{K_0[M]}{K_\infty} \right) \right]^2 \right\}^{-1}$ $K_0 = 5.2 \times 10^{-31} \left(\frac{300}{T} \right)^{3.2}$ $K_\infty = 6.9 \times 10^{-12} \left(\frac{300}{T} \right)^{2.9}$	Atkinson et al. (2006)	(R13)
BrONO ₂ +M→BrO+NO	$2.79 \times 10^{13} e^{(-12389/T)}$	Orlando and Tyndall (1996)	(R14)
BrO+BrO→2Br+O ₂	2.7×10^{-12}	Atkinson et al. (2006)	(R15)
BrO+BrO→Br ₂ +O ₂	$2.9 \times 10^{-14} e^{(840/T)}$	Atkinson et al. (2006)	(R16)
HBr→rainout		Logan et al. (1981)	(R17)
HOBr→rainout		Logan et al. (1981)	(R18)
BrONO ₂ →rainout		Logan et al. (1981)	(R19)
Photolysis Reaction		Reference	Reaction Number
HOBr + <i>hν</i> → Br+OH		Sander et al. (2006)	(R20)
BrONO ₂ + <i>hν</i> → .15(Br+NO ₃)+ .85(BrO+NO ₂)		Sander et al. (2006)	(R21)
Br ₂ + <i>hν</i> → 2Br		Sander et al. (2006)	(R22)
BrO + <i>hν</i> → Br+O		Sander et al. (2006)	(R23)

averaged back to the 1 min merge timeline for analysis. The merged data and selected box model results from ARCTAS are available on a public archive (<http://www-air.larc.nasa.gov/cgi-bin/arcstat-c>).

Sources of uncertainty in model predictions include uncertainties in kinetic and photolytic rate constants, and uncertainties in measurements of constraining observations. Estimates of total model uncertainty are obtained using a Monte Carlo technique and/or a Sensitivity approach. The method

Table 2. Observations used for Model Constraints and/or Predictive Comparisons.

Species	Institution, Instrument	Reference
Physical parameters (e.g., UTC, Latitude, Longitude, Pressure-Altitude, Temperature, Pressure)	NASA DFRC, REVEAL	
Overhead O ₃ Column	NASA, OMI Satellite	http://toms.gsfc.nasa.gov/
Photolysis rates	NCAR, spectral radiometer	Shetter and Muller (1999)
Species for Model Constraint		
H ₂ O, CH ₄ , CO	NASA LaRC, TDLAS	Diskin et al. (2002), Sachse et al. (1987)
O ₃ , NO	NCAR, Chemiluminescence	Weinheimer et al. (1994)
NMHC	UCI, WAS-GC	Blake et al. (2003)
Acetone, methanol	U. Innsbrook, PTR-MS	Wisthaler et al. (2002)
MEK, ethanol	NCAR, GC-MS (TOGA)	Apel et al. (2003)
BrO, SO ₂	Georgia Tech, CIMS	Slusher et al. (2004)
optional constraints (can also be used for predictive comparisons):		
PAN	Georgia Tech, CIMS	Slusher et al. (2004)
HNO ₃	UNH, mist chamber/IC	Scheuer et al. (2003)
CH ₂ O	NCAR, DFGAS	Webring et al. (2007)
Peroxides (H ₂ O ₂ , CH ₃ OOH)	Cal Tech, CIMS	Crounse et al. (2006)
Species for predictive comparisons		
OH, HO ₂	Penn State, LIF (ATHOS)	Faloona et al. (2004)
OH, HO ₂ , HO ₂ +RO ₂	NCAR, CIMS	Cantrell et al. (2003b)

* REVEAL = Research Environment for Vehicle-Embedded Analysis on Linux, OMI = Ozone Monitoring Instrument, TDLAS = Tunable diode laser absorption spectroscopy, WAS-GC = Whole Air Sampling – Gas Chromatography, PTR-MS = Proton Transfer Reaction – Mass Spectrometry, GC-MS = Gas Chromatography – Mass Spectrometry, CIMS = Chemical Ionization Mass Spectrometry, IC = Ion Chromatography, LIF = Laser Induced Fluorescence.

for uncertainty estimation for the LaRC box model is described in more detail in Appendix A.

2.3 Data

The data utilized for model constraint and analysis is presented in Table 2. Key measurements for the high latitude HO_x budget include peroxides (H₂O₂ in particular) from the CIT-CIMS (California Institute of Technology – chemical ionization mass spectroscopy) instrument, which has a 2σ uncertainty of 100 pptv + 50 % of the measurement value (Crounse et al., 2006). Formaldehyde is measured using a difference frequency generation (DFG)/absorption spectroscopy technique (Webring et al., 2007) with a systematic uncertainty at the 2σ level of 12.4 %, and a typical 1 min LOD (2σ) of 22 pptv with degradation of the LOD to ~ 59 pptv during periods of large changes in aircraft cabin pressure (<http://www-air.larc.nasa.gov/cgi-bin/arcstat-c>). Water vapor is obtained from the NASA Langley Research Center DLH (Diode Laser Hygrometer) system with an uncertainty of 10 % (Diskin et al., 2002). The O₃ and NO measurements are obtained from the NCAR four-channel chemiluminescence instrument (Weinheimer et al., 1994) with an 8 % 2σ uncertainty for O₃ and a 16 pptv 2σ

uncertainty for the 60 s average of NO when NO is less than 100 pptv.

Measurements of OH and HO₂ from the Penn State laser induced fluorescence Airborne Tropospheric Hydrogen Oxide Sensor (ATHOS) are available for comparison to model predictions. The HO_x measurements have an uncertainty for both species of ±32 %, and a limit of detection (LOD) of 0.01 pptv for OH and 0.1 pptv for HO₂ (Brune et al., 1999; Faloona et al., 2004). During ARCTAS, the NCAR CIMS instruments also provided measurements of OH and HO₂ (Cantrell et al., 2003b; Mauldin et al., 1999); however due to some irregularities of the inlet heater, the level of coverage from the CIMS instrument was reduced. This analysis uses the ATHOS HO_x measurements. Ren et al. (2012) focuses on a comparison between the two independent measurements of HO_x.

NMHC data are taken from the UC Irvine Whole Air Sampling – Gas Chromatography instrument (Blake et al., 2003), and primary data for acetone and methanol are from the University of Innsbrook Proton Transfer Reaction – Mass Spectrometry instrument (Wisthaler et al., 2002). To maximize the total number of points available for modeling, missing data for acetone, methanol, and NMHCs (with the exception of isoprene) are interpolated from adjacent measurements

within ± 5 min and ± 0.5 km. Any remaining missing acetone and methanol are filled where possible using data from the NCAR Trace Organic Gas Analyzer (TOGA) Gas Chromatography – Mass Spectrometry instrument (Apel et al., 2003); TOGA data are used to fill values 4 % of the time during ARCTAS-A and 8.5 % of time during ARCTAS-B. For the few remaining points with missing acetone or methanol data (0.5 % and 1.5 % during ARCTAS-A and –B), values are filled using observed correlations of PTR-MS acetone or methanol data with CO for each phase of ARCTAS. During ARCTAS-A (spring), the correlations are altitude-independent, while during ARCTAS-B, separate correlations are derived for the lower troposphere where pollution from biomass burning is prevalent ($\text{CO} > 200$ pptv) and for cleaner portions of the troposphere ($\text{CO} < 200$ pptv).

Methyl-ethyl-ketone (MEK) and ethanol data are taken from the TOGA observations. Where data for MEK are missing (< 2 % of the time for ARCTAS-A and 8 % of the time for ARCTAS-B) values are filled using its observed altitude-dependent correlation to acetone for each phase. Missing ethanol (< 1 % of the time for both phases) is filled using its observed altitude-dependent correlation to methanol.

A percentage of the reported measurements of NO are negative, particularly during the summer phase: 6 % of the NO is negative during ARCTAS-A and 20 % is negative during ARCTAS-B (see Fig. 2). For modeling purposes, any 1 min averaged NO less than a threshold value of 1 pptv, including negative values, is set equal to 1 pptv. To test the sensitivity to this choice of minimum threshold, it is varied between 0.1 and 2 pptv. Relative to a 1 pptv threshold, median predictions of OH for these tests vary less than 8 %, and median predictions of HO_2 vary less than 2 %, all of which are less than the relative differences between predictions and measured values at the low NO points. Note that this is not equivalent to estimating the uncertainty in model predictions due to the total uncertainty in NO observations.

Data points identified as stratospherically influenced are removed from this analysis. Points are considered stratospherically influenced when $\text{O}_3 > 100$ ppbv while either $\text{CO} < 100$ ppbv or H_2O is $<$ a threshold value (50 ppmv during ARCTAS-A and 100 ppmv during ARCTAS-B). Thirteen percent of the data during ARCTAS-A are identified and removed, and 4 % of the summer data are removed. Because the altitude range of the C-130 used during TOPSE is limited to less than 8 km, instances of stratospheric influence are rare; about 2 % of the TOPSE-sp data are removed, using the same criteria as for ARCTAS-A. In all cases, the latitude range of the considered data is limited to north of 50° N.

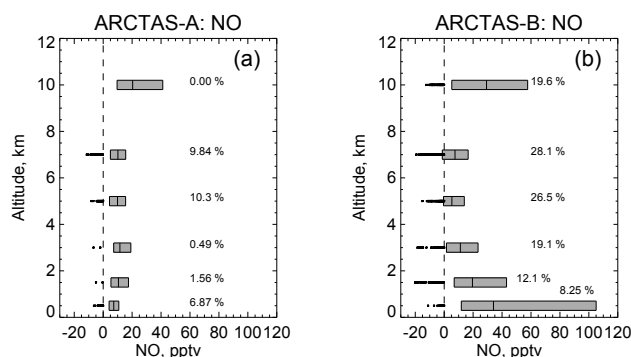


Fig. 2. Range of NO observations during (a) ARCTAS-A and (b) ARCTAS-B for 1-min averages of NO. Bars show the inner 50th percentile range (25–75 %) and vertical lines within bars indicate the median values. Negative values are shown with black points to the left of the dashed line that indicates zero. The percentage of negative values is indicated at each altitude bin.

3 Meteorological and photochemical background at high latitudes

3.1 Meteorology

During ARCTAS-A, the general location of the Arctic front was 60° N (Fuelberg et al., 2010), and most of the aircraft sampling was well north of that. Therefore most of the data was obtained within the extreme cold and dry air of the Arctic air mass. Springtime values for temperature and moisture at high latitudes during TOPSE-sp were comparable to those during ARCTAS-A (Table 3). Alternately, the median sampled latitude during ARCTAS-B was 57° N, while the Arctic front was located well to the north of the bulk of sampled latitudes during that period, leading to higher temperatures and moisture relative to the spring campaigns.

Table 3 also shows the median observed photolysis rates for NO_2 ($J\text{-NO}_2$) and O_3 ($J\text{-O}^1\text{D}$). The near-surface instantaneous observations for $J\text{-NO}_2$ are higher during the spring campaigns (ARCTAS-A and TOPSE-sp) than during summer (ARCTAS-B), while $J\text{-O}^1\text{D}$ shows the opposite tendency. Neglecting transient influences from cloud and aerosols, photolysis is affected by three primary factors: the range of sampled solar zenith angles (SZA), the surface albedo, and the overhead O_3 column. While the range of SZA during the spring is limited to higher values (lower photolysis rates), the persistent snow and ice cover significantly enhances the surface albedo and increases photolysis rates. This albedo-driven increase during spring dominates the difference in rates for $J\text{-NO}_2$. While $J\text{-NO}_2$ is relatively unaffected by changes in the overhead O_3 column, the larger overhead O_3 column during spring (396 DU) relative to summer (316 DU) suppresses $J\text{-O}^1\text{D}$ and offsets its increase due to the albedo enhancement.

Table 3. Median meteorological conditions.

Altitude	Temp (K)	H ₂ O (ppmv)	Inst. J-O ¹ D 10 ⁻⁵ s ⁻¹	Inst. J-NO ₂ 10 ⁻² s ⁻¹
ARCTAS-A > 50° N				
> 8 km	224	80	1.04	1.39
6–8 km	229	148	0.68	1.17
4–6 km	242	296	0.84	1.17
2–4 km	251	614	0.46	0.95
0–2 km	257	1270	0.46	0.91
TOPSE-sp (Mar–Apr) > 50° N				
> 8 km	–	–	–	–
6–8 km	229	161	0.71	1.06
4–6 km	237	225	0.56	1.08
2–4 km	253	869	0.44	0.93
0–2 km	258	1368	0.32	0.79
ARCTAS-B > 50° N				
> 8 km	231	210	1.78	1.25
6–8 km	246	436	2.73	1.22
4–6 km	260	1783	2.14	1.06
2–4 km	273	6292	0.89	0.78
0–2 km	285	9967	1.05	0.51

3.2 Chemical environment

3.2.1 Seasonal comparison

Figures 3–5 show observed profiles of selected species during the spring from ARCTAS-A (dark blue) and from TOPSE-sp (lighter shade of blue). The inner 50th percentile range (25–75 %) within each altitude bin is shown by the colored bars, and the median value is indicated by the vertical lines within the bars. For seasonal comparison, profiles obtained during the summer (ARCTAS-B) are also shown (red).

During ARCTAS-B, there were a number of episodic encounters with fresh biomass burning plumes, and the influence of biomass burning is prevalent to various extents throughout the region. Data points that are clearly within fresh pollution or biomass burning plumes are identified based on at least one of several thresholds being exceeded: CO > 300 ppbv, NO > 500 pptv excluding the upper troposphere, CH₃CN > 300 pptv, or benzene > 150 pptv. Below 2 km, 37 % of the data are identified as fresh plumes (9 % of the data above 2 km). The remaining points represent the “background” shown by the bars in Figs. 3–5. The dashed red line in the figures shows the median profile obtained when all data for ARCTAS-B is used, including that from fresh plumes.

Figure 3a and b reflect the build-up of longer-lived species (e.g., CO and C₃H₈) during winter and early spring. The lifetimes of CO and the NMHC species (Table 4) are dominated by reaction with OH and are 3–4 times longer during spring than summer due to the seasonal variation of OH. Long range transport from middle to high latitudes can be important for

Table 4. Diurnally averaged lifetimes (days) based on model calculations.

Altitude	CO	C ₃ H ₈	C ₂ H ₄	CH ₂ O	H ₂ O ₂	CH ₃ OOH
ARCTAS-A						
> 4 km	220	69	3.8	0.28	3.9	2.4
0–4 km	213	64	3.9	0.38	4.8	3.1
ARCTAS-B						
> 4 km	69	18	1.3	0.16	1.8	1.0
0–4 km	63	14	1.4	0.32	3.0	1.3

these species with lifetimes greater than a few weeks. Fisher et al. (2010) concluded that long-range transport during this time is predominantly from Europe at altitudes near the surface and from Asia throughout the remaining troposphere. Alternately, the dominant impact of local biomass burning emissions during summer (ARCTAS-B) is clearly shown to dominate profiles of the shorter-lived C₂H₄ (Fig. 3c). While middle tropospheric median concentrations of C₂H₄ are similarly low during the two seasons, there is a noticeable increase in the range of values from 2–6 km during ARCTAS-A, and > 8 km during ARCTAS-B. The increased middle tropospheric variability during ARCTAS-A is associated with plumes containing increased CH₃CN, indicating influence from transport of biomass burning emissions, primarily from Asian source regions (Singh et al., 2010; Fisher et al., 2010). During summer, the highest C₂H₄ concentrations at upper altitudes are also associated with higher CH₃CN and CO, consistent with biomass burning pollution. Instances of fast convection of fresh pollution during ARCTAS-B have been identified (e.g., Apel et al., 2012), suggesting that the increased range of values for ethene at upper altitudes during summer is impacted by convection of local biomass burning pollution. O₃ profiles are similar throughout the troposphere during both seasons, with surface values near 30 ppbv increasing to 70 ppbv in the upper troposphere (Fig. 3d). The relatively broad 50th percentile range near the surface during the spring is the result of sampling instances of near-surface halogen-driven O₃ depletion events.

The larger background concentrations and range of NO at low altitudes during ARCTAS-B reflect the pervasive influence from local biomass burning (Fig. 4a). Middle tropospheric concentrations of NO are generally less than 10–20 pptv during both seasons. Browne et al. (2011) determined that both of the NO₂ measurements available during ARCTAS are likely to be contaminated by CH₃O₂NO₂ at low temperatures. Therefore, the NO/NO₂ ratio shown in Fig. 4b is computed using observed NO and model predictions of NO₂. The lower summertime ratio near the surface is impacted equally by the lower near surface J-NO₂ during summer relative to spring (Sect. 3.1) and by the larger summertime concentrations of peroxy radicals, which convert NO to

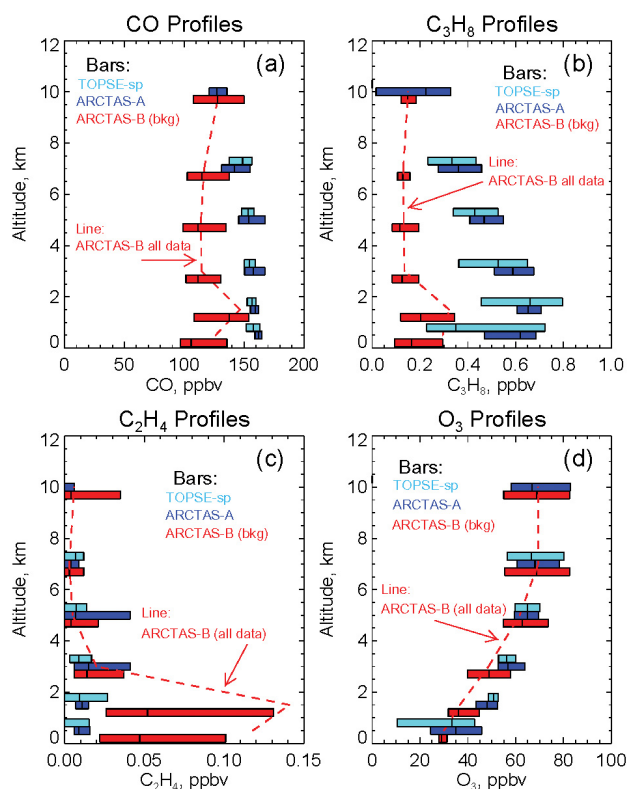


Fig. 3. Profiles of measurements of (a) CO, (b) C₃H₈ (c) C₂H₄ and (d) O₃ during ARCTAS and during TOPSE-sp. Bar plots are as described in Fig. 2. Data for ARCTAS-B shown by the bar plots exclude values identified as within fresh plumes. The dashed lines show the median profile for ARCTAS-B when all data are considered (including fresh plumes).

NO₂. Measurements of gas phase HNO₃ using the University of New Hampshire mist chamber instrument are shown in Fig. 4c, and indicate similar and consistent concentrations in the upper troposphere of less than 100 pptv. The data show flat altitude profiles during spring, and an increase in concentration near the surface during summer.

Figure 5 shows profiles for HO_x precursor reservoirs H₂O₂, CH₃OOH, H₂O₂/CH₃OOH and CH₂O. The relatively short lifetimes for these species shown in Table 4 suggest that long-range transport is unlikely to have a dominant direct impact on concentrations. Concentrations are larger during ARCTAS-B throughout the full extent of the troposphere, reflecting both increased local emission from biomass burning sources and more vigorous photochemical formation in the background atmosphere during the summer.

In comparing the “background” profiles during ARCTAS-B with those using all data, including fresh pollution plumes (dashed red line), it is clear that median values increase in the lowest few km for CO, NMHCs, NO, CH₃OOH and CH₂O as a result of including pollution plumes. HNO₃ and O₃ concentrations, however, are relatively unaffected. This

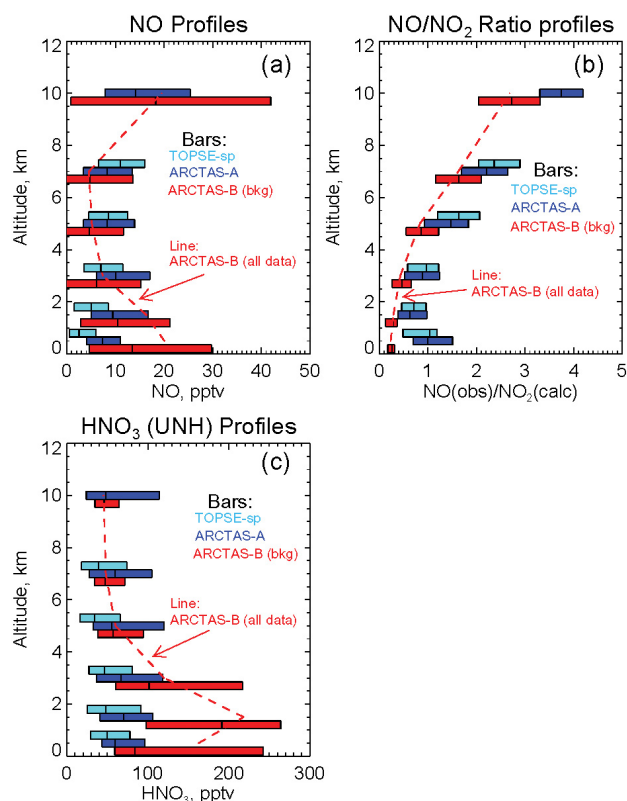


Fig. 4. Profiles of (a) NO, (b) NO/NO₂ and (c) HNO₃ during ARCTAS and during TOPSE-sp. Bar plots and dashed lines are as described in Fig. 3.

implies there is little impact on net O₃ production within the biomass burning plumes, consistent with the analysis of Singh et al. (2010).

3.2.2 TOPSE-sp versus ARCTAS-A

The data in Table 3 and Figs. 3–5 indicate that the air masses sampled during ARCTAS-A and TOPSE-sp were highly similar in meteorological and photochemical characteristics, with the exception of peroxides. Median observations for H₂O₂ during ARCTAS-A were 300–450 pptv throughout the free troposphere, which are 2.5 to 3 times higher than those during TOPSE-sp (100–200 pptv). Measurements from the Atmospheric Chemistry Experiment satellite (ACE; Rinsland et al., 2007) suggest a rapid seasonal change of peroxides in the upper Arctic troposphere between March and May, which would create the possibility of a timing bias between ARCTAS-A and TOPSE; however both of the March and the April profiles from TOPSE remain distinctly lower than that from ARCTAS-A (Fig. 6) and the difference between March and April TOPSE data above 4 km is minimal.

If the differences in H₂O₂ between the campaigns are due to a significant difference in rainout history between TOPSE and ARCTAS-A, these differences should also be reflected in

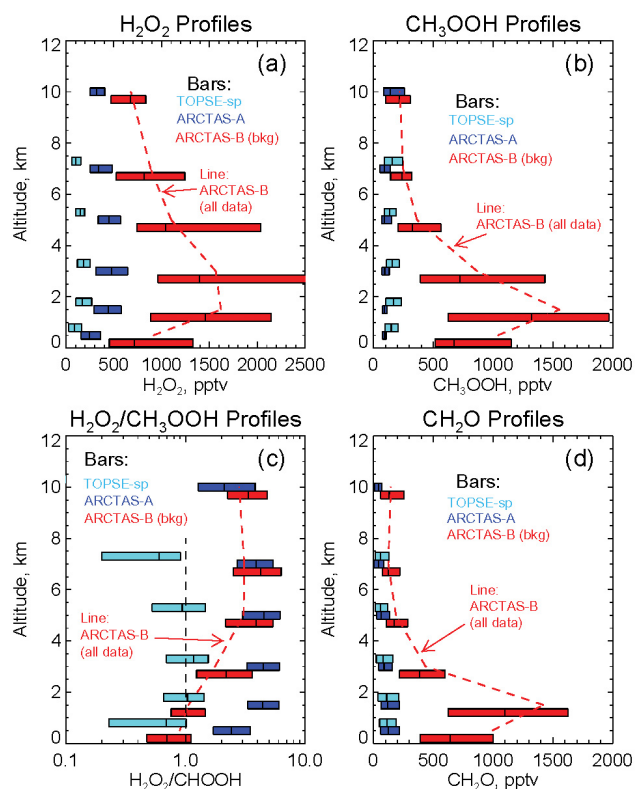


Fig. 5. Profiles of (a) H_2O_2 , (b) CH_3OOH , (c) $\text{H}_2\text{O}_2/\text{CH}_3\text{OOH}$, and (d) CH_2O during ARCTAS-A and -B and during TOPSE-sp. Bar plots and dashed lines are as described in Fig. 3.

other soluble species, notably HNO_3 and to a lesser extent, CH_3OOH . Figure 4c shows slightly lower median values of HNO_3 during TOPSE relative to ARCTAS-A; however, the ambient variability for both campaigns indicated by the 50th percentile ranges is heavily overlapping, while there is a clear separation between peroxide ranges of ambient variability between the two campaigns. Further, a reverse bias is seen for CH_3OOH , with observations during ARCTAS-A being 50–75 % lower than those during TOPSE-sp, which is not supportive of an increased role for rainout during TOPSE. As a result of the different biases for the two peroxides, the $\text{H}_2\text{O}_2/\text{CH}_3\text{OOH}$ ratios in the free troposphere are dramatically different for the two spring campaigns, with values of 3–4 during ARCTAS-A, and values near one during TOPSE-sp. The similarity in CO, NO, and NMHC observations during the two spring campaigns precludes a significant difference due to transport source regions. Given the similarities in physical conditions (H_2O , temperature, radiation) and in other species important in the photochemical budget of peroxides (O_3 , CO, CH_2O), it is difficult to identify a physical reason that peroxides would show such significant differences between the two campaigns.

H_2O_2 measurements during ARCTAS were obtained from both the single-quad and triple-quad implementations of the

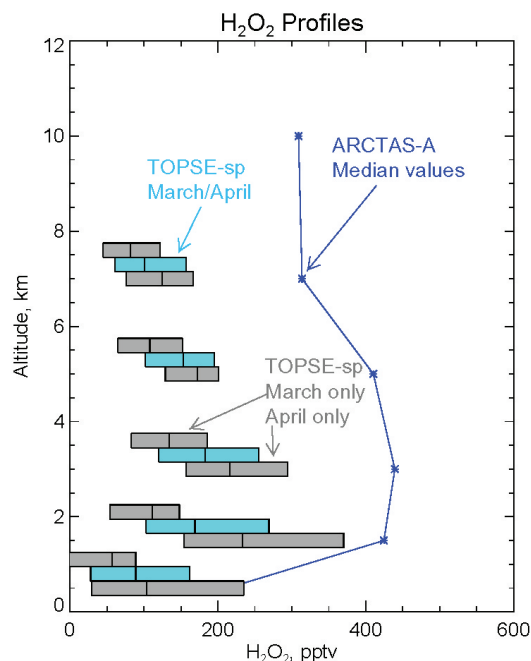


Fig. 6. Median observations of H_2O_2 during ARCTAS-A and during TOPSE-sp, using combined March/April data versus March only and April only.

CIMS instruments, which use independent calibrations for H_2O_2 determinations (Crounse et al., 2006). The two measurements show a high correlation to each other, with no significant bias. The measurements of peroxides during TOPSE-sp were obtained using the University of Rhode Island's instrument utilizing High Performance Liquid Chromatography (URI-HPLC) (Lee et al., 1995; Snow et al., 2003). Both the URI-HPLC instrument and the CIT-CIMS instruments were onboard the DC-8 during NASA's 2004 INTEX-NA campaign (Singh et al., 2006; Snow et al., 2007), during which the two instruments compared well. The median value of H_2O_2 at altitudes > 6 km during INTEX-A was 337 pptv, within the range of concentrations measured during ARCTAS-A. At these lower-concentrations, the fit of CIT-CIMS data to the URI-HPLC data gives a slope of 0.87 and an intercept of 38 pptv. The median ratio between the two peroxide measurements is 0.98, and the r^2 is 0.85, suggesting no bias between the two instruments during INTEX-NA. The cause of the difference in H_2O_2 of several hundred pptv in the free troposphere during ARCTAS-A and TOPSE-sp is unresolved, and, as will be shown, has important implications for conclusions related to the Arctic HO_x budget.

4 Assessment of HO_x photochemistry

For the purpose of a comparison of HO_x observations during ARCTAS to model predictions, the box model is run with full constraints, including CH_2O . The analysis is limited to the

subset of data points that include measurements of the major reservoir HO_x precursors (CH_2O and H_2O_2 , discussed in Sect. 4.1). The other constraints (CH_3OOH , PAN and HNO_3) are used when measurements are available. With these restrictions, there are a total of 1928 ATHOS HO_x measurements available for analysis during ARCTAS-A and 2101 during ARCTAS-B.

4.1 HO_x sources

Because of the rapid cycling between OH and HO_2 , it is useful to examine the source of the combined radicals ($\text{HO}_x = \text{OH} + \text{HO}_2$). Primary sources of HO_x include O_3 photolysis in the presence of water vapor, the photolysis of ketones (particularly acetone), and ozonolysis of alkenes. Additionally, HO_x reservoir species such as H_2O_2 , CH_3OOH , CH_2O and HO_2NO_2 formed during HO_x cycling are a source of HO_x upon photolysis. The source of HO_x originating from multiple species flows through CH_2O (e.g., NMHC, and branches from CH_3OOH and acetone). The constraint of CH_2O to observations in these model simulations, rather than allowing the model to predict concentrations of CH_2O , limits the ability to segregate HO_x sources from CH_2O into the individual initiating species. Figure 7 shows median profiles of the following instantaneous HO_x sources calculated from observations: the primary source stemming from O_3 photolysis, the radical channel of CH_2O photolysis, the branch of CH_3OOH photolysis that does not flow through CH_2O (i.e., that which is not already included implicitly in the calculated source from constrained CH_2O), and the photolysis of H_2O_2 and HO_2NO_2 . The source from ketones and ozonolysis of alkenes are minor contributors and are not shown.

The total HO_x source during ARCTAS-B is nearly an order of magnitude larger than during ARCTAS-A in the boundary layer, and is larger by a factor of 4 in the free troposphere. Dry conditions and low $\text{J-O}^1\text{D}$ photolysis rates during spring result in a suppressed primary source for HO_x from $\text{O}^1\text{D} + \text{H}_2\text{O}$ in the free troposphere, amplifying the importance of the reservoir sources. The flow through CH_2O is the second largest HO_x source in the free and upper troposphere, at about 25 % of the total during both seasons. The source from H_2O_2 is the largest component of the HO_x source in the middle and upper troposphere, at 45 % during spring and 30 % during summer. This emphasizes the importance of differences in H_2O_2 measurements during ARCTAS-A and TOPSE, as it has potential consequences for the total HO_x source.

4.2 Model versus observations of HO_x

Observations of OH and HO_2 are shown by the bar plots in Fig. 8a and b. During ARCTAS-A, concentrations of OH are markedly low. Twenty percent of all OH observations are at LOD (≤ 0.01 pptv), and nearly 40 % of the OH measure-

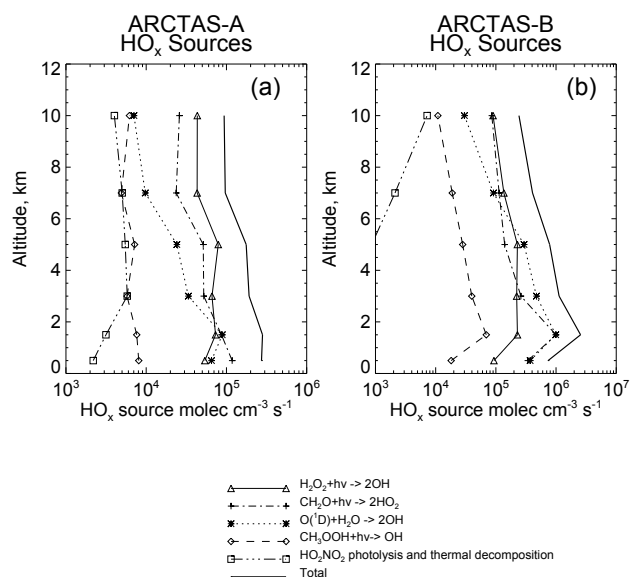


Fig. 7. Gross HO_x production during (a) ARCTAS-A and (b) ARCTAS-B.

ments below 2 km are at LOD. OH concentrations generally increase with altitude. During ARCTAS-B, OH maximizes in the middle troposphere at concentrations more than 4 times larger than those during spring. While springtime values of HO_2 are uniformly low with no vertical gradient (median values are 4 pptv or less), summertime values are largest near the surface (16.7 pptv) and decrease to 7–8 pptv above 8 km.

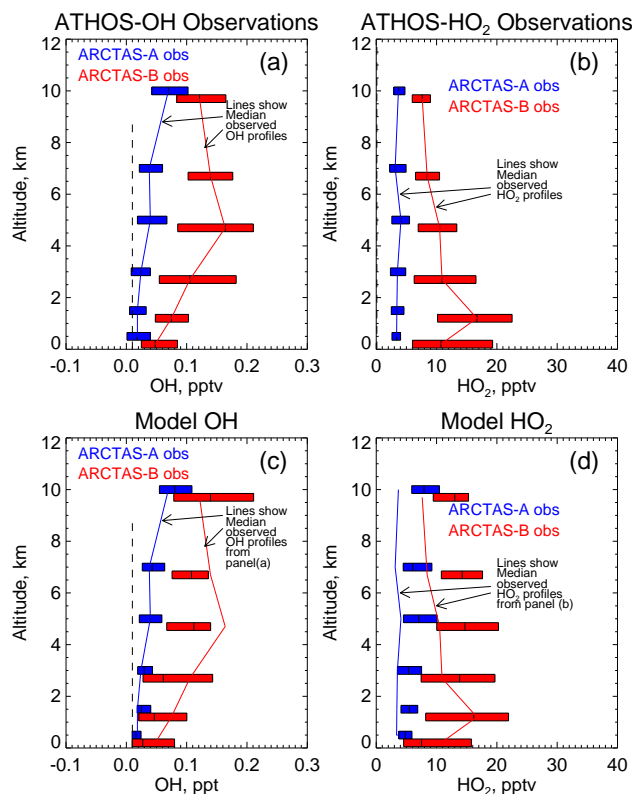
Median model predictions of OH and HO_2 from the fully constrained model are shown by the bars in Fig. 8c and d. The thin solid lines in the figures reproduce the median observed profiles shown in the upper panels for direct comparison. Both the median concentrations and altitude gradient of OH are well represented by the box model during ARCTAS-A, with a median R-Obs/Calc (OH) of 0.96. Alternately, predictions of OH during ARCTAS-B show a gradual increase with altitude, and are generally biased lower than observations. Predictions of HO_2 are significantly and consistently larger than observations throughout the full middle and upper troposphere during both phases. The overestimate of HO_2 persists down to the surface during ARCTAS-A. For further comparison, Fig. 9 shows scatterplots of observed and modeled values for OH and for HO_2 during the two phases. Tables 5 and 6 quantify statistical quantities (median R-Obs/Calc and r^2), calculated using the full set of model/measurement pairs within various altitude bins. The number of OH observations at LOD during ARCTAS-A (often reported as negative values) makes interpretation of R-Obs/Calc problematic. In the cases where both the OH measurement and the model calculation are less than the instrument LOD of 0.01 pptv the two values are assumed to agree and a value of “1” is assigned for R-Obs/Calc. The correlation between measurements and model predictions

Table 5. Median Observed-to-Calculated Ratios and (r^2) for HO_x.

ARCTAS-A		
Altitude	OH (ATHOS) R-Obs/Calc (r^2)	HO ₂ (ATHOS) R-Obs/Calc (r^2)
> 8 km	0.85 (0.64)	0.49 (0.74)
6–8 km	0.91 (0.64)	0.52 (0.85)
4–6 km	1.00 (0.71)	0.58 (0.86)
2–4 km	0.89 (0.38)	0.67 (0.84)
1–2 km	0.74 (0.04)	0.66 (0.58)
0–1 km	1.00 (0.18)	0.71 (0.67)

Table 6. Median Observed-to-Calculated Ratios and (r^2) for HO_x.

ARCTAS-B		
Altitude	OH (ATHOS) R-Obs/Calc (r^2)	HO ₂ (ATHOS) R-Obs/Calc (r^2)
> 8 km	0.88 (0.73)	0.60 (0.76)
6–8 km	1.27 (0.50)	0.61 (0.76)
4–6 km	1.45 (0.61)	0.73 (0.85)
2–4 km	1.32 (0.53)	0.86 (0.82)
1–2 km	1.48 (0.50)	1.10 (0.78)
0–1 km	1.46 (0.59)	1.28 (0.89)

**Fig. 8.** Profiles of observed (a) OH and (b) HO₂ and of model-predicted (c) OH and (d) HO₂ during ARCTAS. Bar plots are as described in Fig. 2. The lines indicate the median observed profiles of OH and HO₂.

(r^2) decreases for OH at low altitudes, particularly during ARCTAS-A. While there is an offset between model predictions and observations of HO₂ throughout most of the domain, the correlation between the two is uniformly high during both phases.

Recent work by Fuchs et al. (2011) show that HO₂ measurement techniques using chemical conversion to OH through the addition of NO such as is used for ATHOS are likely to suffer interferences from aromatic-, alkene-, and

isoprene-based peroxy radicals (RO₂), resulting in a high bias for the HO₂ measurement. Interferences due to RO₂ from smaller alkanes such as methane and ethane are negligible. During ARCTAS, because the HO₂ observations are persistently lower than the model predictions, any interference from RO₂ radicals would only exacerbate the observed to modeled discrepancies. During the summer phase ARCTAS-B and primarily in the boundary layer, about 17 % of the data were comprised of total RO₂ dominated by those from alkene, isoprene, and aromatic chemistry, as predicted by the model. Interestingly, the median R-Obs/Calc for HO₂ for those points is about 25 % larger than that for points where RO₂ is dominated by small alkanes, implying an increase in the observation value relative to the model prediction, consistent with the bias identified by Fuchs et al. (2011). Cases where RO₂ is dominated by alkenes, isoprene and aromatic chemistry are rare in the free troposphere during ARCTAS-B, and negligible during ARCTAS-A.

In addition, recent work by Mao et al. (2012) have recently reported that ground based OH measurements by the Penn State LIF instrument may be subject to an interference related to biogenic volatile organic compounds, particularly at higher temperatures. Very few biogenic hydrocarbons were measured during ARCTAS-A, so this interference should be negligible for that data set. There were more biogenic compounds measured during ARCTAS-B, though at relatively low temperatures; Ren et al. (2012) determine that the level of this interference during ARCTAS cannot be quantified at this time.

Few data sets are available for comparison to these results that include simultaneous measurements of HO_x and its precursors in the free troposphere of the Arctic. A comparison of the ATHOS-LIF HO_x measurements to those from the previously described CIMS instrument which was also on board the DC-8 aircraft during ARCTAS are discussed in detail by Ren et al. (2012). That study shows that CIMS measurements of HO₂ were generally higher than measurements from ATHOS-LIF, with median ratios of [HO₂]_{CIMS}/[HO₂]_{LIF} of 1.65 during ARCTAS-A and 1.28 during ARCTAS-B. This results in a median value for R-Obs/Calc (HO₂) within 10 %

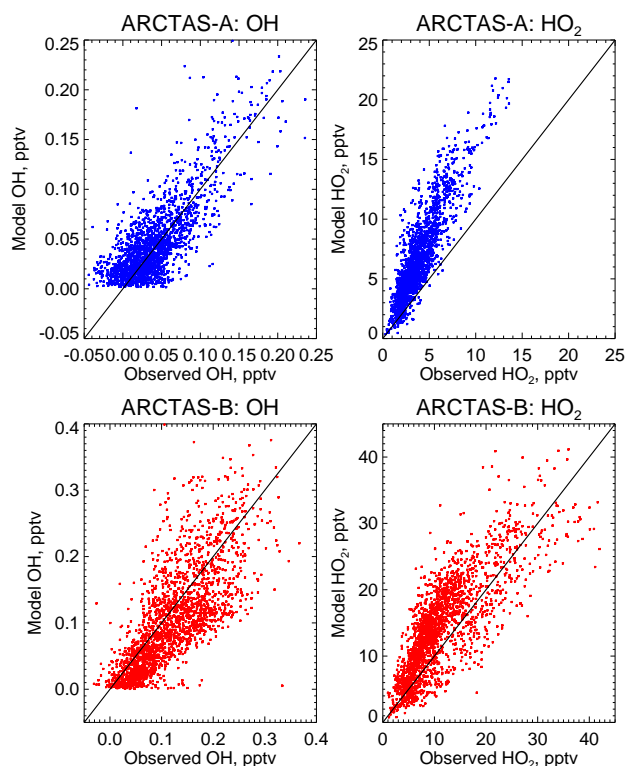


Fig. 9. Scatter plot of observed versus model-predicted (a) OH and (b) HO₂ during ARCTAS-A, and (c) OH and (d) HO₂ during ARCTAS-B. The one-to-one line is shown in black.

of 1 from the surface through 8 km during ARCTAS-A, compared to values from 0.5 to 0.7 for the ATHOS-LIF (HO₂) measurements described above and in Table 3.

The same CIMS instrument was used during the TOPSE campaign, including measurements of HO₂ + RO₂ (Cantrell et al., 2003a), though the number of points available for modeling that include both HO₂ + RO₂ observations and the major precursors (H₂O₂ and CH₂O) is limited to less than 200 points. While the CIMS data gave R-Obs/Calc (HO₂) values near 1 during ARCTAS-A, values of R-Obs/Calc (HO₂ + RO₂) from TOPSE (using the current version of the LaRC model) range from 0.64 at the surface to 0.38 at 6–8 km, more similar to the values using ATHOS-LIF measurements during ARCTAS-A. Note, however, that there is a considerable amount of scatter in this comparison ($r^2 = 0.35$), compared to the highly correlated model-measurements pairs during ARCTAS with $r^2 = 0.75$ to 0.85 in the free troposphere.

4.2.1 OH during ARCTAS-A

To better quantify the amount of scatter in the OH observations during ARCTAS-A, Fig. 10 shows the OH observations plotted as a function of sorted (increasing) model predictions. Sorted model values are shown with black points.

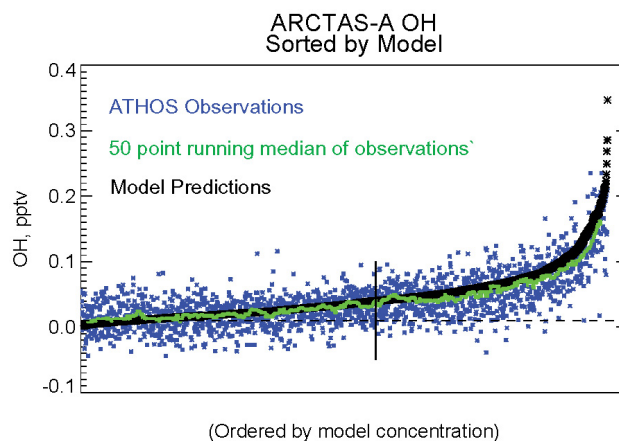


Fig. 10. Observed (blue) and model-predicted (black) concentration pairs of OH during ARCTAS-A sorted by increasing model concentration. The green line shows a 50 point running median of observations along the sorted values.

All data values (blue points) are retained as reported, including those below LOD. A running median of the observations along this sorted series is calculated using a bin size of 50 and is shown with the green line. There is no bias between this running median of observations and the sorted model values at low concentrations. Below an arbitrary threshold value of 0.04 pptv (vertical line in Fig. 10), the median R-Obs/Calc is 1.0, while the model over predicts OH at higher concentrations (median R-Obs/Calc of 0.86). Note that the previously described assumption of R-Obs/Calc = 1 for points where both the model and the observation is at or below LOD affects about 8 % of the points below the threshold. When that assumption is removed, the median R-Obs/Calc changes only slightly to 0.98.

The scatter of observations around the model predictions is large compared to the instrument LOD. For the subset of data below the selected threshold, 98 % (2σ) of the observations are contained within ± 0.05 pptv around model predictions (68 % or 1σ are within ± 0.022 pptv). Because the scatter is symmetric around the model predictions, it is unlikely that a single missing process in the model, such as missing measurements of BrO, can explain the scatter. The 2σ total uncertainties in model predictions of OH are of similar magnitude, ranging from 0.03 to 0.05 pptv (see Appendix A and Table A2). These levels of observational scatter and model uncertainty are at the order of magnitude of the ambient observations. Below 2 km, for example, more than 85 % of the OH observations are less than 0.05 pptv, and nearly 60 % are less than 0.022 pptv. This suggests that at lower altitudes during ARCTAS-A, the practicality of observationally-based analysis using OH data is limited.

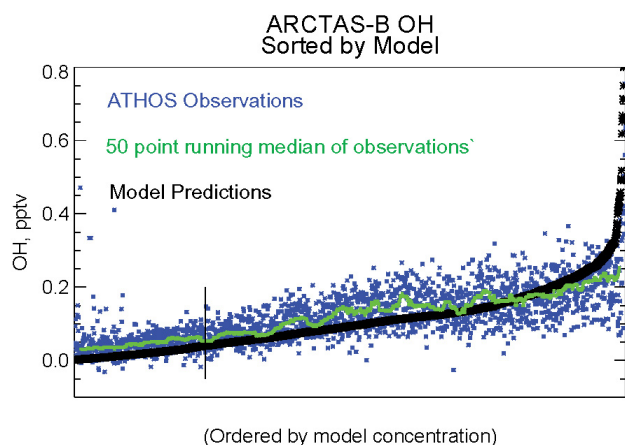


Fig. 11. Observed (blue) and model-predicted (black) concentrations pairs of OH during ARCTAS-B sorted by increasing model concentration. The green line shows a 50 point running median of observations along the sorted values.

4.2.2 OH during ARCTAS-B

During ARCTAS-B, the model persistently under predicts OH for all but the highest altitudes (see Fig. 8c), with an overall R-Obs/Calc of 1.25. The scatter of observations around sorted model concentrations for ARCTAS-B is shown in Fig. 11. In contrast to ARCTAS-A, there is a clear bias toward model under prediction at the lower concentrations (retaining the threshold of 0.04 pptv identified in Sect. 4.3.1), with a median R-Obs/Calc of 2.5. This model under prediction holds throughout most of the range of model predictions, with a switch to over predictions evident only at the highest concentrations. Some recent studies have suggested that at high solar zenith angles, an additional source of OH from the reaction of electronically excited NO_2 with H_2O may result in a source of OH and HONO that rivals the magnitude of the primary source from $\text{O}(^1\text{D}) + \text{H}_2\text{O}$ (Li et al., 2008), although subsequent studies have suggested that the reaction is unlikely to occur in the atmosphere (Carr et al., 2009). However, including this source in the box model made negligible difference in radical production for ARCTAS-B conditions.

The source of OH is strongly impacted by the recycling of HO_2 , which is significantly over predicted at higher altitudes and slightly under predicted at the surface during ARCTAS-B (Fig. 8d). To minimize the impact of imperfect predictions of HO_2 on predictions of OH, it is useful to examine the predicted and observed HO_2/OH ratios. Figure 12a shows that there is a clear tendency of the model to overestimate HO_2/OH at low NO. Further, discussion in Appendix A and Fig. A2 shows that the uncertainty in the NO measurement dominates the uncertainty in model predictions of OH, and that the uncertainty increases with lower NO concentrations. A sensitivity simulation is run whereby NO is universally increased by 16 pptv (the 2σ uncertainty of the NO measure-

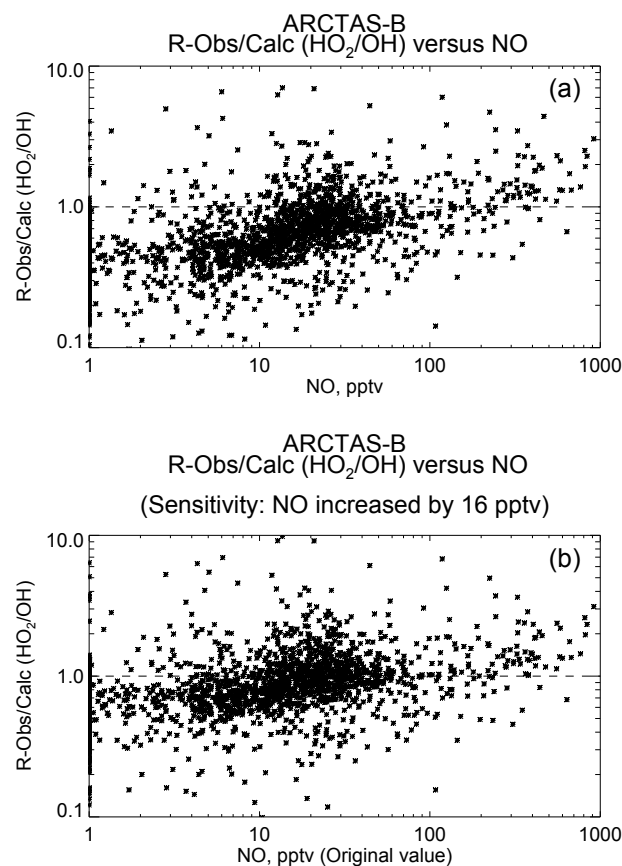


Fig. 12. Observed-to-calculated ratio of the HO_2/OH partitioning during ARCTAS-B as a function of NO. Results from the standard model simulation are shown in (a) and results when NO is universally increased by 16 pptv are shown in (b).

ment at concentrations less than 100 pptv). For this test simulation, the overall median R-Obs/Calc for OH decreases from 1.25 to 0.9 with a dependence on NO concentration. Figure 12b shows the resulting R-Obs/Calc (HO_2/OH). There is currently no reason to suspect a bias in the measurement of NO during ARCTAS-B. However, given the high sensitivity of OH predictions to changes of NO within the bounds of the uncertainty of the measurement, it is difficult to more rigorously diagnose the cause of the persistent under prediction of OH during ARCTAS-B.

4.2.3 Impact of BrO on HO_x during Arctic spring

Halogen chemistry can potentially impact HO_x by altering (decreasing) the HO_2/OH ratio, and also by increasing the total source of HO_x . BrO is formed during the bromine-driven catalytic destruction of O_3 which has been observed over the Arctic (Oltmans and Komhyr, 1986; Barrie et al., 1988). BrO converts HO_2 (and other organic peroxy radicals) to OH via production of HOBr followed by its photolysis

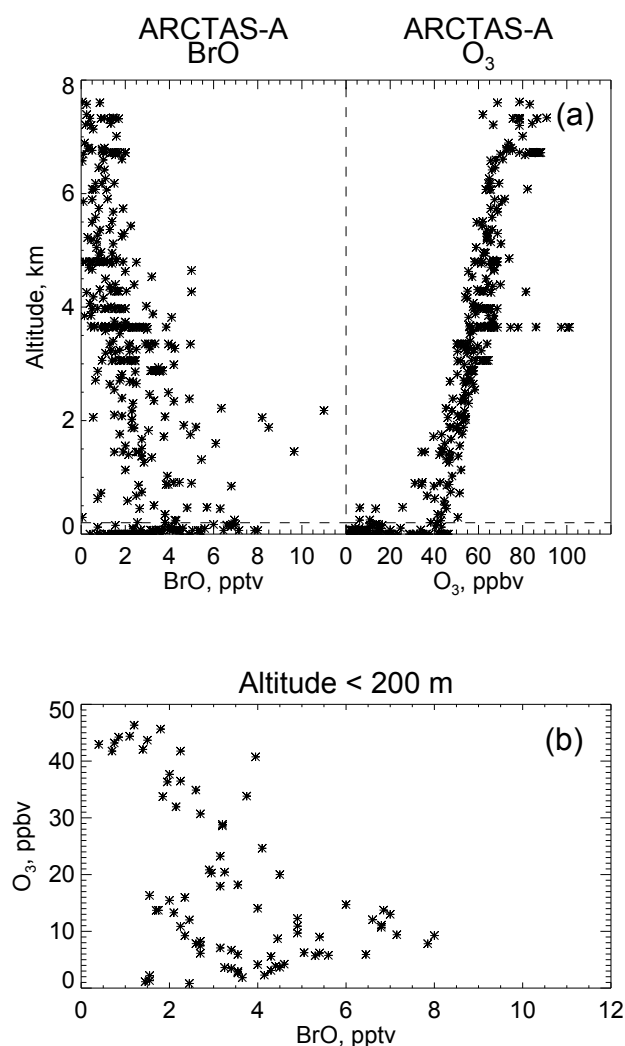
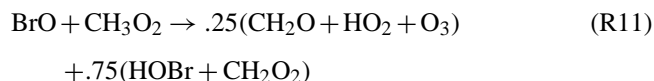
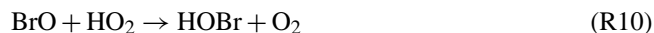
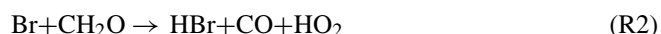


Fig. 13. Observations of BrO and O₃ during ARCTAS-A. Panel (a) shows observed altitude profiles of BrO and O₃ and (b) shows the correlation between BrO and O₃ in the lowest 200 m.

(reactions from Table 1):



In addition to this halogen impact of decreasing the HO₂/OH ratio, the reaction of Br with CH₂O and other aldehydes can serve as a source of HO_x, e.g.,



For most of the ARCTAS data, the source of HO_x from (R2) contributes less than 10 % to the total HO_x source.

However, under conditions where the primary source of HO_x is sufficiently inhibited due to depleted O₃, this bromine-initiated HO_x source can become significant in the relative sense. Additionally, in the presence of high NO (> several hundred pptv) elevated concentrations of the bromine radical (Br) are produced by Reaction (R12) such that the HO₂ source from (R2) can exceed other photochemical HO_x sources:



One of the goals of ARCTAS was to identify observational evidence of these halogen driven impacts on hydrogen radical chemistry. Of the modeled ARCTAS-A data considered in this study, two flights included BrO measurements (423 modeled points), using a CIMS instrument (Neumann et al., 2010). During ARCTAS, the BrO LOD varied but was generally less than 2 pptv. BrO concentrations ranged from up to 8 pptv at the surface to values at LOD in the free troposphere (left panel of Fig. 13a). The right panel in Fig. 13a shows coincident measurements of O₃, and verifies that the aircraft sampling captured some incidences of depleted boundary layer O₃ likely associated with BrO. While the data are influenced by time of day and varying NO_x levels, there is some indication of a general decrease of surface level O₃ with increasing BrO for measurements below 200 m (Fig. 13b).

In its standard configuration, the LaRC steady state model is constrained to measurements of BrO when measurements are available; this approach assumes equilibrium between the active bromine gas-phase species based on the instantaneous value for BrO. Therefore the availability of this measurement allows an estimation of the instantaneous impact of bromine radicals on gas-phase chemistry without the requirement of including details of aqueous-phase processing and bromine activation in the model (e.g., see Liao et al., 2011). Model results including and then neglecting the measurements of BrO are compared to predict the instantaneous impact of bromine on the HO_x budget and cycling in this high latitude environment.

Points with NO > 200 pptv or with O₃ undergoing depletion events (< 15 ppbv) are identified as events that may experience a substantial relative increase in HO_x source due to reaction of Br with aldehydes, e.g., Reaction (R2). The remaining background points encompass more than 85 % of the data. The median relative increase in predicted OH for these background points due to bromine chemistry is 21 % (a 39 % increase for points below 2 km and a 12 % increase in the middle troposphere). However, this translates into very modest absolute concentration increases of < 0.01 pptv (maximum increase is 0.03 pptv). As described in Sect. 4.3.1, available measurements of OH are not sufficient to verify this small impact on OH. The accompanying predicted decrease in background HO₂ due to the halogen chemistry impact on HO₂/OH described above is ~ 4 % (0.22 pptv). This value is significantly less than the total difference between observations and predictions; e.g., for this subset of points,

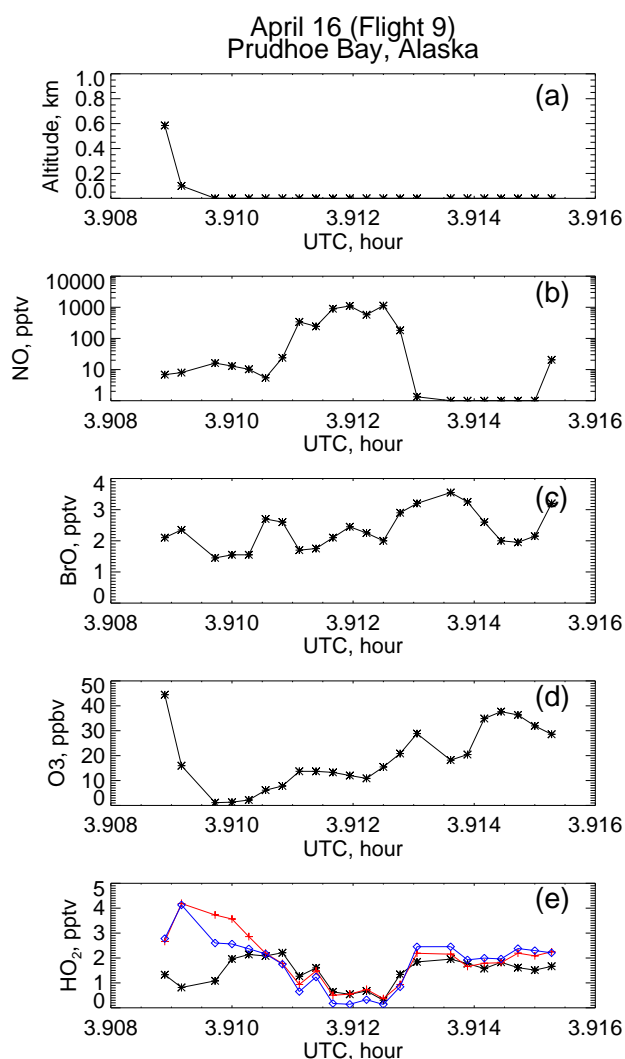


Fig. 14. Case study for impact of bromine on 16 April. Observed time series are shown for (a) Altitude, (b) NO, (c) BrO, and (d) O₃. Observations of HO₂ are shown in panel (e) along with model predictions of HO₂ with and without BrO chemistry.

the median R-Obs/Calc (HO₂) improves from 1.69 to 1.61 when BrO is included in the model calculations. For comparison, Liao et al. (2011) predicted 10–12 % increases in OH due to bromine chemistry over Summit, Greenland during the spring 2007 GSHO_x (Greenland Summit Halogen-HO_x) campaign and 8–10 % decreases in HO₂ + RO₂.

For the 15 points identified as likely HO_x source events due to pollution (NO > 200 pptv), the total HO_x source increases by a factor of 5, resulting in increases of OH and HO₂ on the order of 0.03 pptv and 0.4 pptv respectively. For the points with depleted O₃ (42 points), the total HO_x source increases by 68 % as a result of bromine chemistry, resulting in an OH increase of 0.01 pptv and a HO₂ increase of 0.36 pptv.

Figure 14 is a case study time series of data from 16 April during a very low altitude leg over Prudhoe Bay to illustrate the various impacts of bromine chemistry on the predictions of HO₂ for different chemical environments. Altitude is shown in Fig. 14a, with observations of NO, BrO and O₃ in Fig. 14b–d. The ATHOS measurements of HO₂ for this flight leg are shown in Fig. 14e (black), along with model predictions of HO₂ without bromine chemistry (blue) and with bromine chemistry included (red). Potential HO_x source events are shown at UTC 3.910 (depleted O₃) and in the vicinity of 3.912 (elevated NO). In each case, the prediction of HO₂ is larger when bromine chemistry is included as a result of an increase in the total HO_x source. The agreement with measurements worsens in the O₃ depletion case, but improves to excellent agreement in the high NO case. Background conditions are shown in the vicinity 3.914, where NO drops to less than 10 pptv, and O₃ remains at concentrations > 20 ppbv. In this case, predicted HO₂ decreases with the addition of bromine chemistry as a result of the halogen driven decrease of the HO₂ / OH ratio, improving the agreement between model and observed HO₂.

While there were no measurements of iodine radicals available during ARCTAS, there is recent observational evidence of the presence of IO over isolated regions in the Arctic regions of up to a few pptv (Mahajan et al., 2010). That study suggested that at those concentrations, IO will deplete O₃ at rate comparable to BrO, as well as enhance the effect of bromine-catalyzed O₃ depletion. Modeling studies have indicated that iodine chemistry is also expected to have a significant impact on the HO₂ / OH ratio, parallel to that from BrO (Bloss et al., 2005; Saiz-Lopez et al., 2011).

4.2.4 HO₂

A systematic model over prediction of HO₂ was shown in Fig. 8 and Tables 5 and 6. Figure 15a shows that the R-Obs/Calc (HO₂) is correlated with temperature not only through the two high latitude ARCTAS phases, but also through the portions of the ARCTAS-CARB phase that reached low temperatures (shown in green). The absolute difference between observations and predictions of HO₂ for all three phases are shown in Fig. 15b. For temperatures below 260 K, there is a persistent bias of about 2.5 pptv during ARCTAS-A, and of 5 pptv during ARCTAS-B and ARCTAS-CARB. Stratospheric points for all three phases are shown in the figures with the black plus symbols. There does not appear to be any marked difference in the observation to model comparison for the stratospheric points relative to the tropospheric points. Similar to these box model results, Mao et al. (2010) found an over prediction of HO₂ when comparing results from the chemical transport model GEOS-Chem to ATHOS measurements during ARCTAS-A, and speculated that a temperature-dependent aerosol loss of HO₂ could provide a sufficient additional sink to reconcile HO₂ measurements and theory. The loss of HO₂ to aerosol

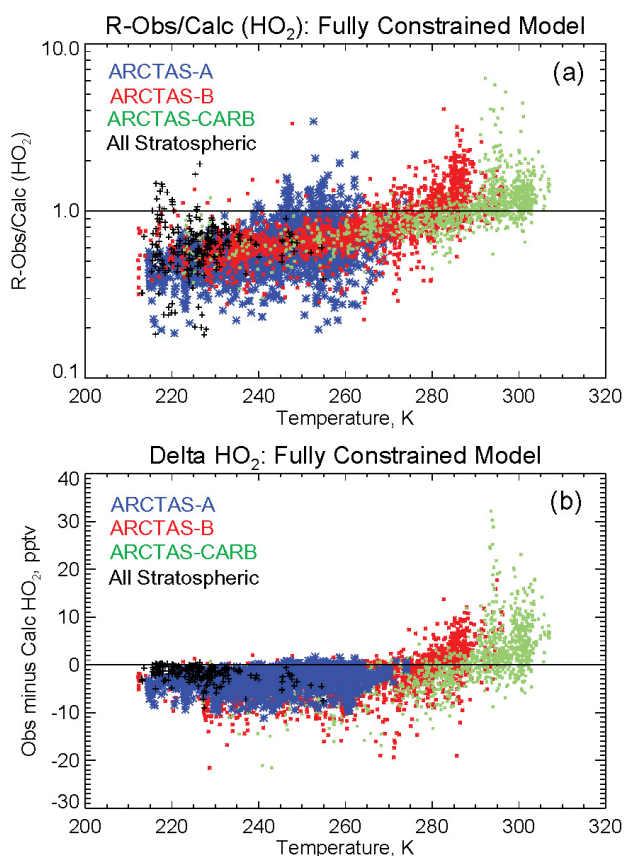


Fig. 15. Model predicted and observation comparisons for HO_2 as a function of temperature. Panel (a) shows R-Obs/Calc (HO_2) for ARCTAS-A, -B and -CARB and (b) shows the difference between observations and model predictions for HO_2 as a function of temperature.

was proposed to proceed as a pseudo first-order loss rate, dependent upon the surface area of the aerosol and a reaction probability that is highly sensitive to temperature and based largely on Thornton et al. (2008). Additionally, Mao et al. (2010) proposed a novel aqueous phase chemistry process that bypasses the formation of H_2O_2 , thus rendering the aerosol reaction a terminal loss of HO_y .

The results from Mao et al. (2010) are based on three-dimensional model predictions of physical parameters and chemical precursor fields, and are useful for assessing relative influences on the chemical system as a whole. However, the HO_x precursor fields generated by global models are not sufficient to perform a direct measurement-to-model assessment of HO_x . The only way to determine whether a terminal loss of HO_2 to aerosol is sufficient to reconcile in-situ observations of HO_x with theory is to directly consider the observed precursor fields. Measurements of HO_x , its precursors, and species and parameters impacting its loss (i.e., aerosol surface area and temperature) are used here with the observationally constrained box model to examine the

proposed temperature-dependent heterogeneous loss of HO_2 . The loss rate is calculated using an aerosol surface area density (SAD) and a reaction probability (γ):

$$\text{HO}_2 \text{ loss rate} = \frac{\text{SAD}}{\left\{ \frac{4}{\gamma\omega} + \frac{r_p}{D_g} \right\}} \quad (1)$$

where ω is the temperature-dependent mean molecular speed of HO_2 , r_p is the particle radius, and D_g is the diffusion coefficient for HO_2 . Unfortunately, measurements of aerosol SAD from the DC-8 are not available for altitudes above about 3 km during ARCTAS because the Ultra High Sensitivity Aerosol Spectrometer instrument was not functional above this altitude. Measurements of aerosol scattering @550 nm were available on the DC-8, however, and are used here as a proxy to estimate aerosol SAD. The relationship between SAD and aerosol scattering @550 nm can be obtained for altitudes up to 8 km during ARCTAS using measurements from the suite of instruments on board the P3-B aircraft (operated by the Hawaii Group for Environmental Aerosol Research; Clark, 1991); this relationship is then applied to observations of aerosol scattering @550 nm obtained from the DC-8 to obtain estimates of SAD values consistent with the DC-8 data set.

The aerosol SAD measurements from the P3-B are shown in Fig. 16a and b in blue. Below 4 km, local fire emissions result in very high aerosol SAD values (off scale in Fig. 16b) but as will be shown, a heterogeneous loss to aerosol at the lower altitudes has little impact on HO_2 due to the magnitude of competing gas phase losses of HO_x at these altitudes. Note that these values for aerosol SAD assume dry particles, and therefore have an uncertainty associated with them in the presence of sufficient relative humidity (RH). For these P3-B data, 3/4 of the points above 6 km are at less than 56 % RH. For these dry conditions, the uncertainty in SAD is likely less than about a factor of 2. Figure 16c and d show the linear fits obtained using the correlation for SAD values $< 30 \text{ cm}^2 \text{ cm}^{-3}$ and aerosol scattering @550 nm using measurements from the P3-B. Resulting estimates for SAD for the DC-8 using that linear fit applied to DC-8 measurements of aerosol scattering @550 are indicated with the white bars in Fig. 16a and b. Aerosol SAD estimates for the DC-8 are similar to those from the P3-B in both median and range. For comparison, the predicted aerosol SAD from the GEOS-Chem global model for the same subset of DC-8 points is also shown in the figure (gray bars), with median values up to a factor of ~ 2 larger than those from the airborne measurements. Given the uncertainty related to RH, the difference between the estimates from in-situ data and those from GEOS-Chem can be interpreted as a reasonable range of values for SAD in the high latitude upper troposphere.

To estimate values for the reaction probability (γ) for the HO_2 aerosol loss in Eq. (1), a temperature-dependent estimate is based on that described in Thornton et al. (2008), assuming a pH of 5 and a particle radius of $0.2 \mu\text{m}$. The

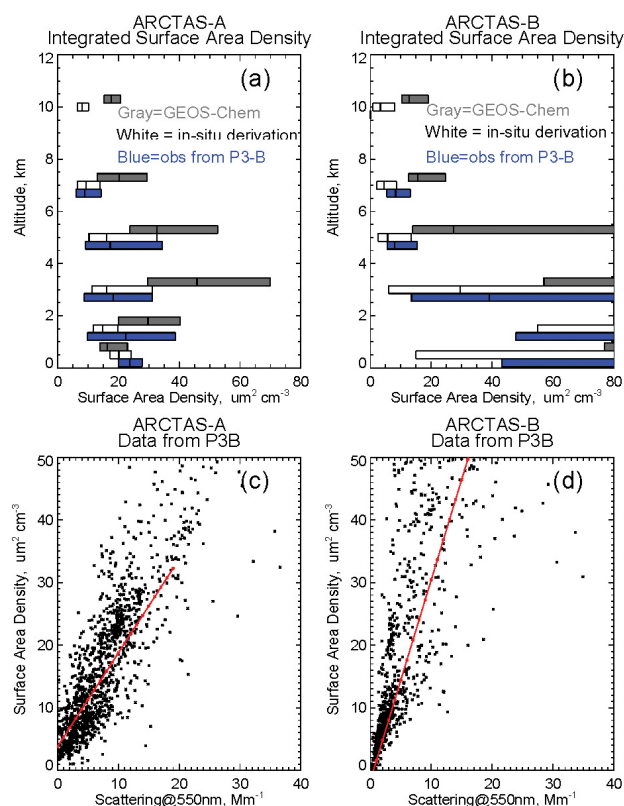


Fig. 16. Integrated surface area density (SAD) and scattering @550 nm during ARCTAS. Altitude profiles of SAD are shown for (a) ARCTAS-A and (b) ARCTAS-B. Bars show values of SAD obtained from P3-B observations, from derivations using a correlation to DC-8 observations of scattering @550 nm, and from calculations using the GEOS-Chem model. Bar plots are as described in Fig. 2. The correlation between measurements of SAD and scattering @550 nm from the P3-B are shown for (c) ARCTAS-A and (d) ARCTAS-B.

calculated reaction probability ranges from 0.06 near the surface to 0.7 in the upper troposphere. The assumption of a particle radius (r_p) = $0.2 \mu\text{m}$ in Eq. (1) will overestimate the loss rate when larger particles dominate; P3-B size distribution data suggest that above 6 km, ~60 % of the integrated surface area is from particles < $0.2 \mu\text{m}$ radius, on average. This in-situ based estimate of the terminal aerosol loss for HO_2 is shown in Fig. 17a and b (white bars) along with the corresponding loss calculated by GEOS-Chem along the DC-8 flight tracks (gray bars). The GEOS-Chem calculation employs a similar approach to that used here, but integrates throughout the full spectrum of the model-generated particle size distribution information. The two estimates for the HO_2 loss rate to aerosol are generally consistent, with that predicted by GEOS-Chem somewhat larger, particularly during summer, driven by the larger SAD in GEOS-Chem. For the fully constrained box model test used here, this aerosol loss for HO_2 will only be effective at decreasing concen-

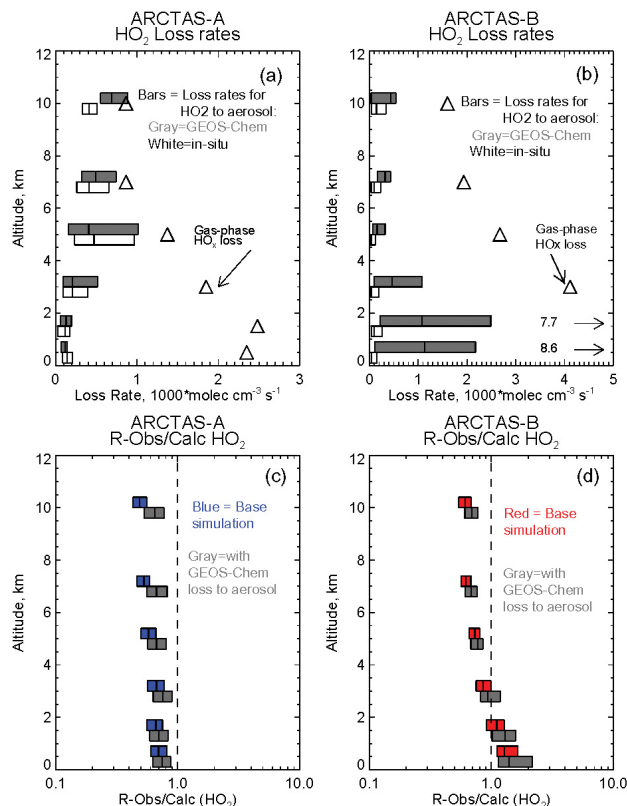


Fig. 17. Impact of including a heterogeneous loss rate of HO_2 to aerosol on predictions of HO_2 . Altitude profiles of the loss rate of HO_2 to aerosol calculated in GEOS-Chem and from using in-situ observations are shown for (a) ARCTAS-A and (b) ARCTAS-B. Predictions of the gas-phase loss of HO_2 using the LaRC box model and in-situ observations are shown for comparison. Altitude profiles of the observed-to-calculated ratios of HO_2 from simulations that do and do not include the heterogeneous loss of HO_2 to aerosol are shown for (c) ARCTAS-A and (d) ARCTAS-B.

trations of HO_2 if the magnitude of the estimated loss rate is competitive with the gas phase losses of HO_x , shown by the open triangles in Fig. 17a and b (including the HO_2 self reaction, reaction of HO_2 with RO_2 to form organic peroxides, and reaction of OH with NO_2 to form HNO_3). For altitudes near the surface, the gas phase losses clearly dominate the estimates for aerosol loss. In the upper troposphere, the aerosol loss approaches values of the gas-phase loss during ARCTAS-A, and reaches 20 to 30 % of the gas-phase loss during ARCTAS-B.

To test the impact of including this HO_2 loss to aerosol using the observationally constrained box model, the larger loss rates from GEOS-Chem are adopted to give an upper bound estimate of the HO_2 loss. The loss rate is assumed to be terminal, as in Mao et al. (2010). The resulting changes in the R-Obs/Calc HO_2 ratio are shown in Fig. 17c and d, where the blue (ARCTAS-A) and red (ARCTAS-B) bars show the standard model results, and the gray bars show results when the

HO₂ loss to aerosol adopted from GEOS-Chem is included. In the upper troposphere for ARCTAS-A, the predicted HO₂ concentration decreases by ~23 % as a result of the loss to aerosol, though it is clearly not sufficient to reconcile the discrepancy with observations. Differences in the absolute concentrations of HO₂ predicted here and those by GEOS-Chem in Mao et al. (2010) stem from distributions of CH₂O, H₂O₂, H₂O and J(O¹D) that are lower in GEOS-Chem than were observed during ARCTAS. The impact during ARCTAS-B is more subdued as expected, due to the relatively larger competing gas-phase HO_x losses. In both phases, a significant bias toward over prediction remains, particularly at upper altitudes, with the median R-Obs/Calc (HO₂) above 4 km equal to 0.66 during ARCTAS-A and equal to 0.72 during ARCTAS-B. The HO₂ loss to aerosol in the upper troposphere would need to be three times larger than those adopted from GEOS-Chem during ARCTAS-A and six times larger during ARCTAS-B in order to predict HO₂ at the approximate magnitude of observations. Because the reaction probabilities at the high altitude colder temperatures are already large, this would suggest that the increases would need to come largely from higher values of aerosol SAD. Because GEOS-Chem values of SAD used in this calculation of the loss rate are approximately twice as large as the dry-particle in-situ derivations, this would in turn imply that values of SAD would be required to be 6 to 12 times larger than the in-situbased estimate. Increases of this order of magnitude are generally outside of the range of uncertainty associated with measurements for this region.

4.2.5 Coupling HO_x and HO_x precursors

Figures 18 and 19 show predictions of HO₂, OH, CH₂O and H₂O₂ from a suite of model simulations. The standard fully constrained model simulation (heavy solid line), and that including the loss of HO₂ to aerosol (heavy dash-dot line) have been discussed previously. The figures also show several additional partially unconstrained simulations that test the ability of model photochemistry to sustain observed values of HO_x reservoir precursors (peroxides and CH₂O) by predicting one or more of those species from model photochemistry rather than constraining to observations. Predictions of peroxides are highly sensitive to the model assumptions for rainout and deposition loss; within the lowest km the H₂O₂ lifetime due to surface deposition dominates its near-surface total loss rate, and up to 4 km the assumed rainout lifetime is approximately equal to the photochemical lifetime for H₂O₂. Because the history of physical loss due to rainout and/or deposition for any given air mass is highly uncertain, additional model simulations are performed that neglect surface deposition and rainout loss (dry simulations) in order to provide a range of predictions that bracket likely scenarios for these losses. The figures also show median observed values from ARCTAS with $\pm 2\sigma$ instrument uncertainties (asterisks and horizontal lines), and median observations from TOPSE-sp

are shown with the open triangles in Fig. 18 for comparison to ARCTAS-A.

The collective group of model predictions shows a persistent over prediction of HO₂ during both seasons. For both ARCTAS-A and -B, the prediction of HO₂ that is most consistent with observations comes from a dual unconstrained model simulation (thin black line), in which both peroxides and CH₂O are predicted from steady state. Above the boundary layer, predictions of HO₂ from this simulation are 30–40 % lower than those from the standard fully constrained run during ARCTAS-A, and they are 10–25 % lower during ARCTAS-B. However, the predictions of H₂O₂ and CH₂O from this simulation (thin black lines in Figs. 18c, d and 19c, d) are well below ARCTAS observations, emphasizing the inconsistency between measurements of HO_x and of its precursors during ARCTAS. The predictions of H₂O₂ during ARCTAS-A are of similar magnitude to those measured during TOPSE-sp, and it can be argued that both lie just within the range of ARCTAS H₂O₂ instrument 2 σ uncertainty. Whether differences are within or outside of the range of measurement uncertainty, however, it is clear that these differences in predicted and measured HO_x precursor concentrations have important implications for the HO_x budget.

As discussed previously, predictions of OH during ARCTAS-A are consistent with observations in the median, but there is a clear under prediction of OH during ARCTAS-B for all but the highest altitudes (Figs. 18b and 19b). The blue thin dotted line in Fig. 19b shows OH predictions for ARCTAS-B from the sensitivity run using the fully constrained standard model where NO was universally increased by its 2 σ uncertainty of 16 pptv (discussed in Sect. 4.3.2). This sensitivity run reproduces median observed OH concentrations in the middle and lower troposphere, while changes to HO₂ are minor (less than a few percent). This emphasizes the sensitivity of OH predictions to uncertainties in the NO measurement during ARCTAS.

Simulations were also run whereby the constraint of a single HO_x precursor is individually relaxed; i.e., peroxides are constrained to observations while CH₂O is predicted (green lines, see Figs. 18d and 19d) and CH₂O is constrained to observations while peroxides are predicted (purple lines, see Figs. 18c and 19c). The corresponding dashed green and purple lines show results from the dry simulations, whereby the rainout loss for the predicted precursor is neglected. In general, the impact on CH₂O predictions due to peroxide constraint is small. Predictions increase and are closer to observations above 8 km during ARCTAS-A and below 4 km during ARCTAS-B, however CH₂O predictions remain significantly lower than observations throughout most of the free troposphere during both phases, part (Figs. 18d and 19d). Alternately, when CH₂O is held constrained to observed values, the predicted H₂O₂ from the rainout and the dry simulations bracket observations for all but the very highest altitudes (> 8 km) during both phases. Thus, while the model is unable to reproduce any consistency between observed

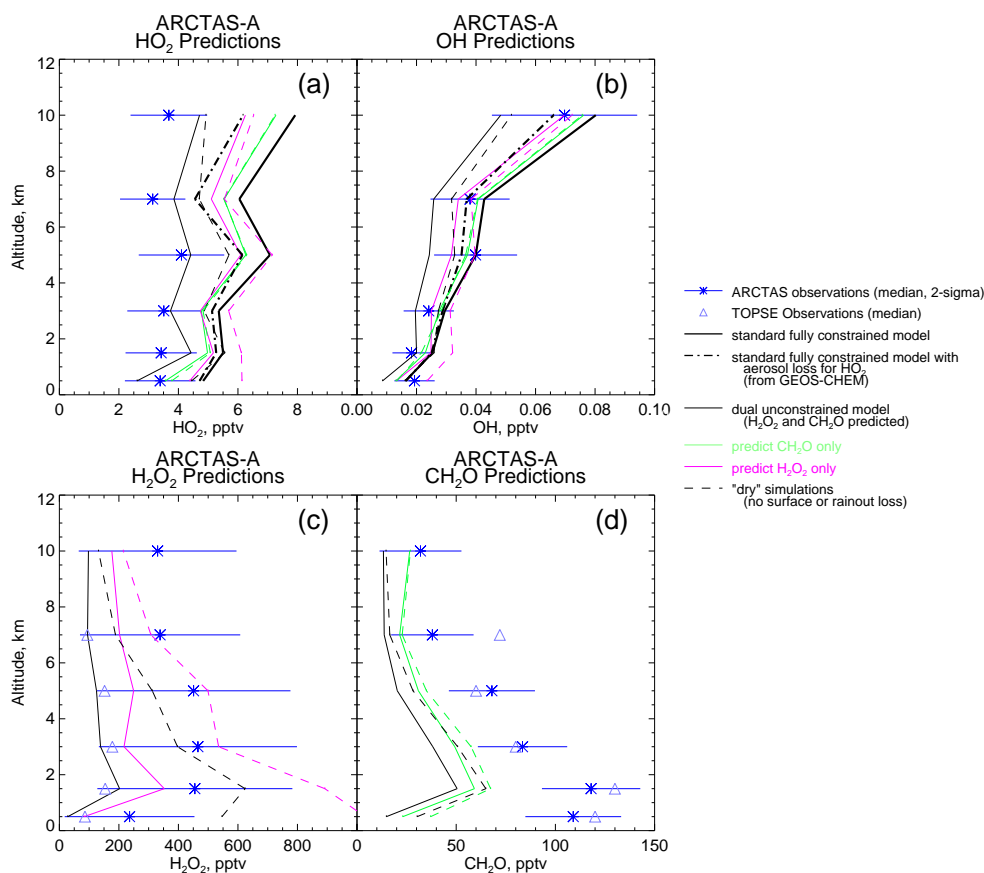


Fig. 18. Altitude profiles for observations and model predictions of (a) HO_2 , (b) OH , (c) H_2O_2 and (d) CH_2O during ARCTAS-A, with model predictions from several different permutations of the LaRC box model. Asterisks show the median observations, and the associated horizontal blue lines indicate the 2σ uncertainty in the observation. Median observations of H_2O_2 and CH_2O from TOPSE-sp are shown with triangles in (c) and (d).

concentrations of HO_x and of its precursors, it is possible to argue there is some consistency between measurements of CH_2O and H_2O_2 when CH_2O is forced to observations.

Observed levels of CH_2O cannot be explained by model photochemical theory, and the diurnally averaged lifetime of CH_2O is short enough to preclude a significant source from middle latitude transport (6–10 h during ARCTAS-A and 3–10 h during ARCTAS-B). Sources that are not included in the box model such as emission from the snowpack and/or direct emission from fires may explain a portion of the model under predictions at the lowest altitudes, but these surface sources are unlikely to have a persistent impact throughout the extent of the troposphere during ARCTAS-A. The instances of convection observed during ARCTAS-B are a likely mechanism for transport of surface levels of CH_2O into the upper troposphere. In addition, convective transport of very short lived precursors such as isoprene can have an impact on upper tropospheric CH_2O concentrations that persist beyond the observable levels of the precursors; however the model under predictions of CH_2O are persistent and not

limited to convective events. Fried et al. (2003) suggested that a temperature-dependent branching of $\text{CH}_3\text{O}_2 + \text{HO}_2$ to directly produce CH_2O may be important in cold temperatures (Elrod et al., 2001). This branching ratio varies from 10–15 % at the surface to 25 % in the upper troposphere for ARCTAS conditions. However including this branch in the model chemistry did not substantially change predicted concentrations of CH_2O .

Figure 20 shows that model predictions of acetaldehyde (CH_3CHO) during ARCTAS are lower than both of two independent measurements using the PTRMS and TOGA instruments. To investigate the magnitude of an additional photochemical source of CH_2O from oxidation of observed levels of acetaldehyde, the model is run in a mode to predict CH_2O while retaining all other constraints with the additional constraint of acetaldehyde. The higher values of CH_3CHO from PTRMS are used to give upper bound estimates. Predicted CH_2O increases by less than 3 pptv during ARCTAS-A, except for altitudes > 8 km, where predicted CH_2O increases by 7.5 pptv to explain approximately half of the discrepancy

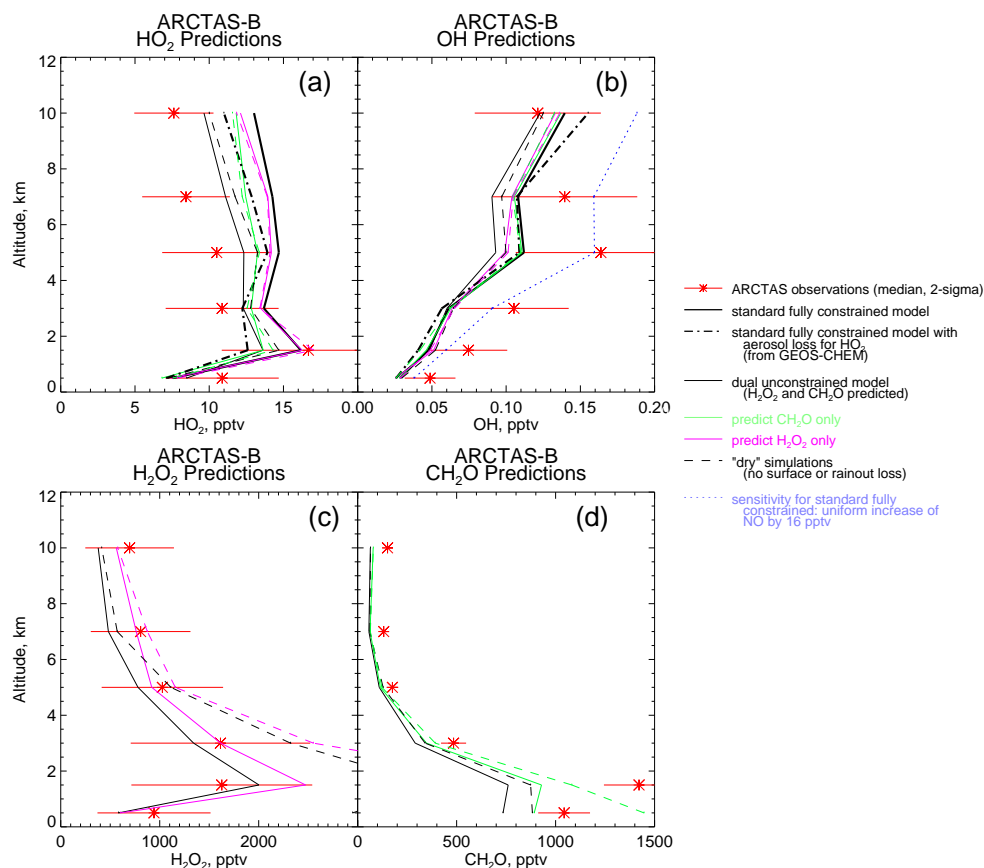


Fig. 19. As in Fig. 18, but for ARCTAS-B.

between the model and observations. During ARCTAS-B, predicted CH_2O increases by 20 pptv for altitudes above 2 km, explaining between 25–60 % of the discrepancy.

The estimate of an additional flux of CH_3CHO required to reproduce the larger observations measured by PTRMS ranges from 35–90 pptv day^{-1} during ARCTAS-A, and up to several hundred pptv day^{-1} during ARCTAS-B. While the lifetime of acetaldehyde is longer than that of formaldehyde (1–3 days during spring and ~ 1 day during summer), it is not long enough to support a sustained significant transport flux of this magnitude. Kwan et al. (2006) speculate that oxidation of organic aerosols could be a source of oxygenated volatile organic compounds (OVOCs), and propose that up to 70 pptv C day^{-1} (equivalent to 35 pptv day^{-1} CH_3CHO) is possible in the upper troposphere over North America. Another possible source of acetaldehyde might be due to oxidation of unmeasured higher hydrocarbons. The origin of such a source that is pervasive throughout the high latitude troposphere is unknown.

5 O₃ budget

The diurnally averaged gross photochemical formation and destruction of O_3 during the two ARCTAS phases is shown in Fig. 21a and b by the bars on either side of the zero line. For ARCTAS-B, the results shown are limited to the “background” points, described in Sect. 3.2. The median net O_3 photochemical tendencies are shown by the blue (ARCTAS-A) and red (ARCTAS-B) lines. O_3 gross formation ranges from 0.4–0.8 ppbv day^{-1} during ARCTAS-A, with the upper value occurring at 1–4 km. This rate is in general agreement with the range of calculations for TOPSE (Cantrell et al., 2003a; Stroud et al., 2004). The net photochemical production of O_3 during spring is zero throughout most of the troposphere, with a small net positive production at highest altitudes of 0.2 ppbv day^{-1} . This supports the conclusions of TOPSE, that in order to support the springtime build up of O_3 at high latitudes, a combination of both transport of O_3 from middle latitudes and gross photochemical production is required. During summer (ARCTAS-B), the background data shows a gross production of O_3 in the boundary layer and at the highest altitudes 2–4 ppbv day^{-1} , with a net photochemical production of 1–2 ppbv day^{-1} . The middle troposphere

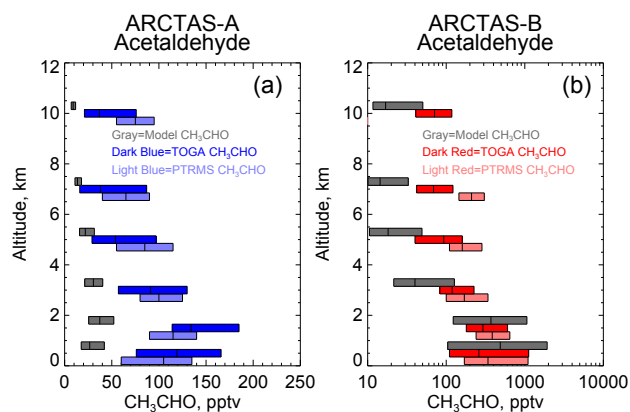


Fig. 20. Altitude profiles of observations and model predictions of acetaldehyde during (a) ARCTAS-A and (b) ARCTAS-B. Bar plots are as described in Fig. 2.

is characterized by net photochemical destruction of about 1 ppbv day^{-1} .

Given the persistent model over prediction of HO_2 , it is instructive to determine if and how much the O_3 formation and destruction rates during ARCTAS would vary if observed HO_2 were considered, rather than model-calculated values. Figure 21c and d show the revised gross production and destruction rates, and the net production calculated using the observed HO_2 values. Throughout the free troposphere during both phases and extending to the surface during ARCTAS-A, gross production rates are 25–50 % lower when using observed HO_2 (see Table 7). Gross destruction is similarly reduced, so that differences in the net O_3 production rate are negligible.

6 Summary

Observations obtained during ARCTAS were analyzed using the observationally constrained NASA Langley Research Center photochemical box model in order to assess the tropospheric photochemical cycling occurring over high latitudes and its impact on the O_3 budget. At high latitudes and particularly during the spring, low radiation, cold temperatures, and dry conditions suppress photochemistry such that concentrations of many of the radicals and precursor species are very low. The resulting relative uncertainties in measurements and model predictions are sufficiently large so as to preclude a rigorous photochemical assessment.

While model predictions of OH during the spring (ARCTAS-A) are in general agreement with measurements ($R\text{-Obs}/\text{Calc} = 0.96$), observations of OH are frequently at LOD. The low concentrations in the boundary layer and lower troposphere are shown to have observational scatter and model prediction uncertainties that are at the order of magnitude of the ambient concentrations, limiting the usefulness of further observational analysis. Alternately, dur-

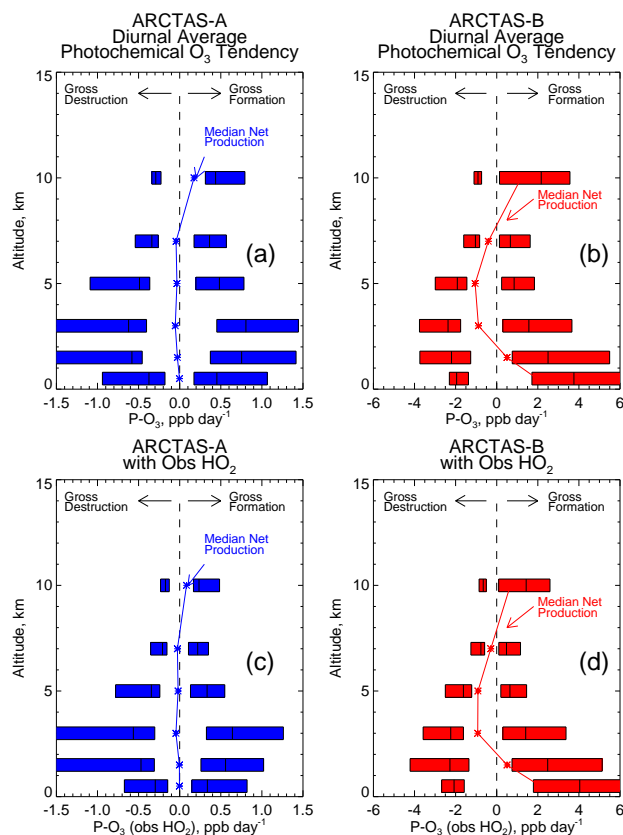


Fig. 21. Altitude profiles of diurnally averaged model calculated gross formation and destruction and net production of O_3 during (a) ARCTAS-A and (b) ARCTAS-B. Bar plots are as described in Fig. 2. Panels (c) and (d) are for the diurnally averaged gross formation and destruction and net production of O_3 using observed HO_2 rather than model predictions.

ing summer (ARCTAS-B), concentrations of OH are four times larger than during spring, but predictions of OH are persistently lower than observations for all but the highest OH concentrations ($R\text{-Obs}/\text{Calc} = 1.25$). The $R\text{-Obs}/\text{Calc}$ HO_2/OH ratio shows a clear trend with NO with largest over-predictions at low NO concentrations. The uncertainty in model predictions of OH associated with uncertainties in observational constraints is dominated by the NO measurement uncertainty, and is largest at low values of NO. Predicted OH is consistent with measurements (within 10 %) if NO is increased uniformly within the bounds of its 2σ uncertainty, though there is no reason to suspect a bias in NO measurement at this time.

The largest sources of HO_2 in the middle and upper troposphere during ARCTAS are photolysis of H_2O_2 and CH_2O . Predictions of HO_2 are up to a factor of two larger than measurements when H_2O_2 and CH_2O are constrained to their observed values, highlighting the inconsistency between measurements of HO_2 and of its reservoir precursor species within the context of the box model mechanism. The

Table 7. Changes in O₃ gross formation when using observed HO₂.

Altitude	ARCTAS-A Percent, (ppbv day ⁻¹)	ARCTAS-B Percent, (ppbv day ⁻¹)
> 8 km	-46 % (-0.20)	-34 % (-0.73)
6–8 km	-40 % (-0.14)	-28 % (-0.19)
4–6 km	-31 % (-0.15)	-24 % (-0.20)
2–4 km	-20 % (-0.16)	-10 % (-0.15)
1–2 km	-26 % (-0.20)	-0.6 % (-0.02)
0–1 km	-26 % (-0.12)	+7.6 % (+0.28)

temperature dependent terminal loss of HO₂ to aerosol proposed by Mao et al. (2010) decreased model predictions of HO₂ by ~23 % during ARCTAS-A, but was not sufficient to reconcile the differences between measured and predicted HO₂.

A comparison of measurements during ARCTAS-A and at high latitudes during the spring portion of the 2000 TOPSE field campaign revealed strikingly consistent measurements of temperature, water vapor, CO, NO, NMHCs, and CH₂O. However, differences were apparent in measurements of peroxides, with those during TOPSE several hundred pptv lower than during ARCTAS. A reverse bias is seen for CH₃OOH, with observations during ARCTAS-A 50–70 % lower than during TOPSE. The similarity in physical conditions and photochemical precursors precludes obvious differences in transport, rainout, or in the photochemical budget terms as a cause of the difference. The cause of this difference in peroxides remains unresolved and has important implications for the Arctic HO_x budget.

The box model photochemistry alone is unable to explain observed concentrations of CH₂O or H₂O₂ during ARCTAS; observations are larger than box model predictions by factors of ~2–3 during spring and by 50–200 % during summer. Predictions of HO₂ resulting from these combined lower model predicted precursor values are more consistent with observed HO₂, further highlighting the inconsistency between the measurements of HO_x and its precursors. Sensitivity simulations were also run where CH₂O was predicted while keeping peroxides constrained to observations, and vice versa, with peroxides being predicted while using constraint of observed CH₂O. Photochemistry resulting from observed concentrations of peroxides is unable to reproduce observed values of CH₂O. However, when the model is constrained to observed CH₂O, predictions of H₂O₂ using a range of rainout loss rates bracket observations.

Observations of acetaldehyde are larger than model predictions, and can provide an additional photochemical source of CH₂O that can explain up to half of the discrepancy between the model and measurements for portions of the troposphere. A source to explain larger acetaldehyde concentrations could be a result of oxidation of organic aerosols

Table A1. 1σ uncertainties for selected input constraints on 60 s time average.

Constraint	1σ uncertainty for 60 s average for ARCTAS
O ₃	4.3 % (for O ₃ ≤ 10 ppbv) 4 % (for O ₃ > 10 ppbv)
CO	2 %
NO	8 pptv (for NO < 100 pptv) 10 pptv (for NO 100–1000 pptv) 60 pptv (for NO > 1000 pptv)
CH ₃ OOH	33 pptv + 27 % (for H ₂ O 0–230 ppmv) 33 pptv + (−6.07+13.87log(H ₂ O)) % (for H ₂ O > 230 ppmv)
H ₂ O ₂	67 pptv + 27 % (ARCTAS-A) 67 pptv + 33 % (ARCTAS-B)
H ₂ O	Greater of 5 % or 1 ppmv
CH ₂ O	$\sqrt{(12.2 \% [\text{CH}_2\text{O}])^2 + (\text{LOD}_{(\sim 22 \text{ ppt})})^2}$

and/or unmeasured NMHC species, but the origin of such a precursor(s) that is pervasive throughout the higher latitudes is unknown.

Gross O₃ production during ARCTAS-A maximizes at 0.8 ppbv d⁻¹ from 1–4 km, which is generally consistent with estimates from TOPSE. The net photochemical tendency is zero throughout the troposphere, indicating that transport of O₃ from middle latitudes is necessary to explain the springtime buildup of O₃ over high latitudes. During ARCTAS-B, there is a gross photochemical O₃ production of 2–4 ppbv d⁻¹ in the boundary layer and at highest altitudes, with net photochemical tendencies of < 2 ppbv day⁻¹, while the middle troposphere is a net photochemical sink for O₃. The use of observed concentrations of HO₂ rather than model predictions decreased the gross photochemical formation rates above the boundary layer by 25–50 %. However, because the gross destruction of O₃ is reduced by a similar amount, the net photochemical production was relatively unaffected by the choice of modeled or measured HO₂.

Appendix A

Model uncertainty analysis

Sources of uncertainty in model predictions include uncertainties in kinetic and photolytic rate constants, and uncertainties in measurements of constraining observations. One method of estimating the model uncertainty uses a Monte Carlo approach, which can be executed for typical meteorological and chemical conditions for a region(s) of interest. Median observed values are found for lower (0–4 km), middle (4–8 km) and upper (> 8 km) altitudes during each of the two ARCTAS phases. For each of these six sets of median conditions, the model uncertainty due to kinetics was calculated by running 2500 simulations whereby each of 105 model kinetic reaction rates and 16 photolytic rates was randomly and independently varied within its referenced 1σ

Table A2. 2σ Uncertainty in model predictions for ARCTAS-A (Fully Constrained Model).

	SENSITIVITY APPROACH	MONTE CARLO APPROACH	MONTE CARLO APPROACH	MONTE CARLO APPROACH
Altitude	Median 2σ $\text{HO}_{2\text{calc}}$ Obs. Constraint (Relative)	2σ $\text{HO}_{2\text{calc}}$ Obs. Constraint Relative (pptv)	2σ $\text{HO}_{2\text{calc}}$ Kinetics Relative (pptv)	2σ $\text{HO}_{2\text{calc}}$ Combined Relative
> 8 km	.24	.25 (2.13)	.29 (2.39)	.38
4–8 km	.22	.21 (1.72)	.26 (2.19)	.33
0–4 km	.20	.14 (0.88)	.24 (1.52)	.28
Altitude	Median 2σ OH_{calc} Obs. Constraint (Relative)	2σ OH_{calc} Obs. Constraint Relative (pptv)	2σ OH_{calc} Kinetics Relative (pptv)	2σ OH_{calc} Combined Relative
> 8 km	.60	.56 (0.04)	.41 (0.03)	.69
4–8 km	.64	.58 (0.03)	.36 (0.02)	.68
0–4 km	.68	.50 (0.03)	.31 (0.01)	.59

Table A3. 2σ Uncertainty in model predictions for ARCTAS-B (Fully constrained Model).

	SENSITIVITY APPROACH	MONTE CARLO APPROACH	MONTE CARLO APPROACH	MONTE CARLO APPROACH
Altitude	Median 2σ $\text{HO}_{2\text{calc}}$ Obs. Constraint (Relative)	2σ $\text{HO}_{2\text{calc}}$ Obs. Constraint Relative (pptv)	2σ $\text{HO}_{2\text{calc}}$ Kinetics Relative (pptv)	2σ $\text{HO}_{2\text{calc}}$ Combined Relative
> 8 km	.16	.14 (2.60)	.28 (5.01)	.31
4–8 km	.14	.12 (2.22)	.25 (4.56)	.28
0–4 km	.08	.09 (1.52)	.23 (4.02)	.25
Altitude	Median 2σ OH_{calc} Obs. Constraint (Relative)	2σ OH_{calc} Obs. Constraint Relative (pptv)	2σ OH_{calc} Kinetics Relative (pptv)	2σ OH_{calc} Combined Relative
> 8 km	.34	.33 (0.08)	.35 (0.08)	.48
4–8 km	.44	.51 (0.08)	.33 (0.05)	.61
0–4 km	.32	.29 (0.02)	.33 (0.03)	.44

uncertainty (Sander et al., 2006; Atkinson et al., 2005). The resulting range in predictions of radical species was used to find the model predictive uncertainty (converted to 2σ) due to kinetic uncertainties.

To evaluate uncertainty due to constraining species, another set of Monte Carlo simulations was performed for the six sets of median input conditions, whereby each of seven selected constraining species was randomly and independently varied within the 1σ measurement uncertainty for a 60 s average (Table A1). The resulting 2σ uncertainties in model predictions of OH, HO_2 are shown in Tables A2 and A3 for ARCTAS-A and ARCTAS-B. A total model uncer-

tainty is estimated using a quadrature sum of these two components.

Because these uncertainty estimates are based on a limited set of input conditions, they should be interpreted as representative of a general bulk analysis of the data. Uncertainties for the individual data points will vary, depending upon the meteorology and chemical regime (i.e., dominant reactions). Rigorous calculation of uncertainties for each individual data point using the Monte Carlo approach would require an exorbitant amount of computing time. To estimate the predictive uncertainty for an individual data point, a “Sensitivity” approach may be employed, whereby each data point is run N times ($N = N_{\text{con}} + N_{\text{kin}}$), where N_{con} is the number of

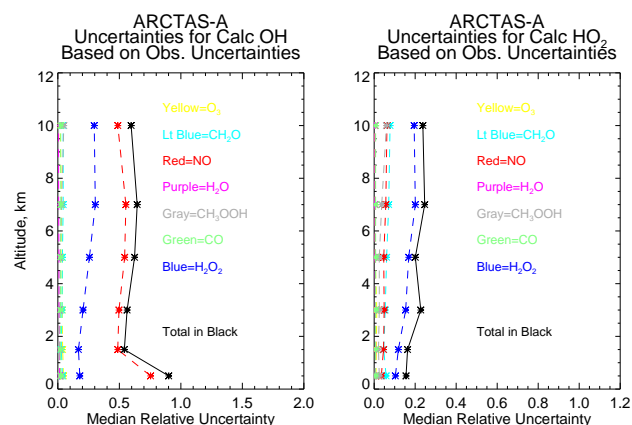


Fig. A1. Altitude profiles of the median relative uncertainty in prediction of (a) OH and of (b) HO₂ during ARCTAS-A that is due to the uncertainty in observations of constraining species.

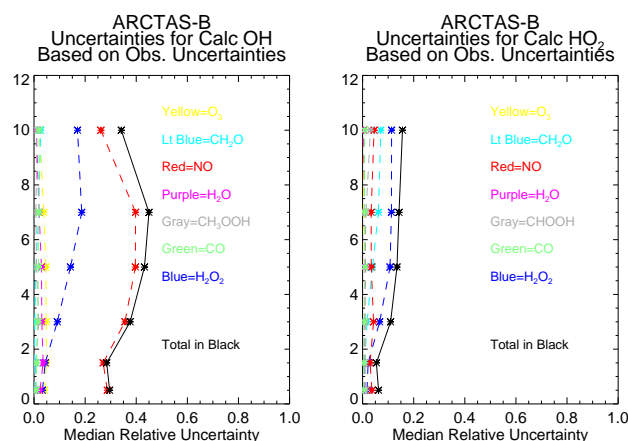


Fig. A2. As for Fig. A1, but for ARCTAS-B.

observational constraints selected to consider, and N_{kin} is the number of kinetic reactions selected to consider. For these sensitivity simulations, the component of interest (an observational constraint or a reaction rate) is increased by its 1σ uncertainty, and the absolute value of the relative difference in radical predictions is calculated. A quadrature sum of uncertainties obtained from each considered component gives an estimate of the total combined uncertainty for that individual data point. For comparison to the Monte Carlo results, Tables A2 and A3 also show the medians of the combined uncertainties obtained using the sensitivity approach for the 7 constraints listed in Table A1.

Figures A1 (ARCTAS-A) and A2 (ARCTAS-B) show the individual contributions to the observational constraint uncertainty for prediction of OH and HO₂ from seven selected measurements. The dominant measurement uncertainty impacting OH prediction is clearly NO, while H₂O₂ dominates the uncertainty in prediction of HO₂.

Acknowledgements. The ARCTAS mission was funded by the NASA Global Tropospheric Chemistry Program, the NASA Radiation Sciences Program, and the California Air Resources Board. We gratefully acknowledge the NASA aircraft crews and science team. The two anonymous reviewers for this manuscript are also thanked.

Edited by: W. T. Sturges

References

- Apel, E. C., Hills, A. J., Lueb, R., Zindel, S., Eisele, S., and Riemer, D. D.: A fast-GC/MS system to measure C₂ to C₄ carbonyls and methanol aboard aircraft, *J. Geophys. Res.*, 108, 8794, doi:10.1029/2002JD003199, 2003.
- Apel, E. C., Olson, J. R., Crawford, J. H., Hornbrook, R. S., Hills, A. J., Cantrell, C. A., Emmons, L. K., Knapp, D. J., Hall, S., Mauldin III, R. L., Weinheimer, A. J., Fried, A., Blake, D. R., Crounse, J. D., Clair, J. M. St., Wennberg, P. O., Diskin, G. S., Fuelberg, H. E., Wisthaler, A., Mikoviny, T., Brune, W., and Riemer, D. D.: Impact of the deep convection of isoprene and other reactive trace species on radicals and ozone in the upper troposphere, *Atmos. Chem. Phys.*, 12, 1135–1150, doi:10.5194/acp-12-1135-2012, 2012.
- Atkinson, R., Baulch, D. L., Cox, R. A., Crowley, J. N., Hampson, R. F., Hynes, R. G., Jenkin, M. E., Rossi, M. J., Troe, J., and IUPAC Subcommittee: Evaluated kinetic and photochemical data for atmospheric chemistry: Volume II – gas phase reactions of organic species, *Atmos. Chem. Phys.*, 6, 3625–4055, doi:10.5194/acp-6-3625-2006, 2006.
- Atlas, E. L., Ridley, B. A., and Cantrell, C. A.: The tropospheric ozone production about the Spring Equinox (TOPSE) Experiment: Introduction, *J. Geophys. Res.*, 108, 8353, doi:10.1029/2002JD003172, 2003.
- Barrie, L. A., Bottenheim, J. W., Schnell, R. C., Crutzen, P. J., and Rasmussen, R. A.: Ozone destruction and photochemical reactions at polar sunrise in the lower Arctic atmosphere, *Nature*, 334, 138–141, 1988.
- Blake, N. J., Blake, D. R., Swanson, A. L., Atlas, E., Flocke, F., and Rowland, F. S.: Latitudinal, vertical and seasonal variations in C1–C4 alkyl nitrates in the troposphere over the Pacific Ocean during PEM-Tropics A and B: Oceanic and continental sources, *J. Geophys. Res.*, 108, 8806, doi:10.1029/2002JD003367, 2003.
- Bloss, W. J., Lee, J. D., Johnson, G. P., Sommariva, R., Heard, D. E., Saiz-Lopez, A., Plane, J. M. C., McFiggans, G., Coe, H., Flynn, M., Williams, P., Rickard, A. R., and Fleming, Z. L.: Impact of halogen monoxide chemistry upon boundary layer OH and HO₂ concentrations at a coastal site, *Geophys. Res. Lett.*, 32, L06814, doi:10.1029/2004GL022084, 2005.
- Brock, C. A., Radke, L. F., Lyons, J. H., and Hobbs, P. V.: Arctic hazes in summer over Greenland and the North American Arctic. I: Incidence and origins, *J. Atmos. Chem.*, 9, 129–148, doi:10.1007/BF00052828, 1989.
- Browne, E. C., Perring, A. E., Wooldridge, P. J., Apel, E., Hall, S. R., Huey, L. G., Mao, J., Spencer, K. M., Clair, J. M. St., Weinheimer, A. J., Wisthaler, A., and Cohen, R. C.: Global and regional effects of the photochemistry of CH₃O₂NO₂: evidence from ARCTAS, *Atmos. Chem. Phys.*, 11, 4209–4219, doi:10.5194/acp-11-4209-2011, 2011.

- Brune, W. H., Tan, D., Faloona, I. F., Jaeglé, L., Jacob, D. J., Heikes, B. G., Snow, J., Kondo, Y., Shetter, R., Sachse, G. W., Anderson, B., Gregory, G. L., Vay, S., Singh, H. B., Davis, D. D., Crawford, J. H., and Blake, D. R.: OH and HO₂ chemistry in the North Atlantic free Troposphere, *Geophys. Res. Lett.*, 26, 3077–3080, 1999.
- Cantrell, C. A., Mauldin, L., Zondlo, M., Eisele, F., Kosciuch, E., Shetter, R., Lefer, B., Hall, S., Campos, R., Ridley, B., Walega, J., Fried, A., Wert, B., Flocke, F., Weinheimer, A., Hannigan, J., Coffey, M., Atlas, E., Stephens, S., Heikes, B., Snow, J., Blake, D., Blake, N., Katzenstein, A., Lopez, J., Browell, E. V., Dibb, J., Scheuer, E., Seid, G., and Talbot, R.: Steady state free radical budgets and ozone photochemistry during TOPSE, *J. Geophys. Res.*, 108, 8361, doi:10.1029/2002JD002198, 2003a.
- Cantrell, C. A., Edwards, G. D., Stephens, S., Mauldin, R. L., Zondlo, M. A., Kosciuch, E., Eisele, F. L., Shetter, R. E., Lefer, B. L., Hall, S., Flocke, F., Weinheimer, A., Fried, A., Apel, E., Kondo, Y., Blake, D. R., Blake, N. J., Simpson, I. U. J., Bandy, A. R., Thornton, D. C., Heikes, B. G., Singh, H. B., Brune, W. H., Harder, H., Martinez, M., Jacob, D. J., Avery, M. A., Barrick, J. D., Sachse, G. W., Olson, J. R., Crawford, J. H., and Clarke, A. D.: Peroxy radical behavior during the Transport and Chemical Evolution over the Pacific (TRACE-P) campaign as measured aboard the NASA P-3B aircraft, *J. Geophys. Res.*, 108, 8797, doi:10.1029/2003JD003674, 2003b.
- Carr, S., Heard, D. E., and Blitz, M. A.: Comment on “Atmospheric Hydroxyl Radical Production from Electronically Excited NO₂ and H₂O”, *Science*, 324, 336, doi:10.1126/science.1166669, 2009.
- Chen, G., Davis, D., Crawford, J., Hutterli, L. M., Huey, L. G., Slusher, D., Mauldin, L., Eisele, F., Tanner, D., Dibb, J., Buhr, M., McConnell, J., Lefer, B., Shetter, R., Blake, D., Song, C. H., Lombardi, K., and Arnoldy, J.: A reassessment of HO_x South Pole chemistry based on observations recorded during ISCAT 2000, *Atmos. Environ.*, 38, 5451–5461, 2004.
- Clark, A. D.: A Thermo-optic technique for in-situ analysis of size-resolved aerosol Physicochemistry, *Atmos. Environ.*, 25A, 635–644, 1991.
- Comiso, J. C., Parkinson, C. L., Gersten, R., and Stock, L.: Accelerated decline in the Arctic sea ice cover, *Geophys. Res. Lett.*, 35, L01703, doi:10.1029/2007GL031972, 2008.
- Crawford, J., Davis, D., Olson, J., Chen, G., Liu, S., Gregory, G., Barrick, J., Sachse, G., Sandholm, S., Heikes, B., Singh, H., and Blake, D.: Assessment of upper tropospheric HO_x sources over the tropical Pacific based on NASA GTE/PEM data: Net effect on HO_x and other photochemical parameters, *J. Geophys. Res.*, 104, 16255–16273, 1999.
- Crounse, J. D., McKinney, K. A., Kwan, A. J., and Wennberg, P. O.: Measurement of gas-phase hydroperoxides by chemical ionization mass spectrometry, *Anal. Chem.*, 78, 6726–6732, 2006.
- Diskin, G. S.: Open-path Airborne Tunable Diode Laser Hydrometer, Diode Lasers and Applications in Atmospheric Sensing, SPIE Proceedings 4817, A. Fried, editor, 196–204, 2002.
- Elrod, M. J., Ranschaert, D. L., and Schneider, N. L.: Direct kinetic study of the temperature dependence of the CH₂O branching channel for the CH₃O₂+HO₂ reaction, *Int. J. Chem. Kinet.*, 33, 363–376, 2001.
- Emmons, L. K., Hess, P., Klonecki, A., Tie, X., Horowitz, L., Lamarque, J.-F., Kinnison, D., Brasseur, G., Atlas, E., Brownell, E., Cantrell, C., Eisele, F., Mauldin, R. L., Merrill, J., Ridley, B., and Shetter, R.: Budget of tropospheric ozone during TOPSE from two Chemical transport models, *J. Geophys. Res.*, 108, 8372, doi:10.1029/2002JD002665, 2003.
- Evans, M. J., Jacob, D. J., Atlas, E., Cantrell, C. A., Eisele, F., Flocke, F., Fried, A., Mauldin, R. L., Ridley, B. A., Wert, B., Talbot, R., Blake, D., Heikes, B., Snow, J., Walega, J., Weinheimer, A. J., and Dibb, J.: Coupled evolution of BrO_x-ClO_x-HO_x-NO_x chemistry during bromine-catalyzed ozone depletion events in the arctic boundary layer, *J. Geophys. Res.*, 108, 8368, doi:10.1029/2002JD002732, 2003.
- Faloona, I., Tan, D., Leshner, R. L., Hazen, N. L., Frame, C. L., Simpas, J. B., Harder, H., Martinez, M., DiCarlo, P., Ren, X., and Brune, W. H.: A Laser-induced Fluorescence Instrument for Detecting Tropospheric OH and HO₂: Characteristics and Calibration, *J. Atmos. Chem.*, 47, 139–167, 2004.
- Fisher, J. A., Jacob, D. J., Purdy, M. T., Kopacz, M., Le Sager, P., Carouge, C., Holmes, C. D., Yantosca, R. M., Batchelor, R. L., Strong, K., Diskin, G. S., Fuelberg, H. E., Holloway, J. S., Hyer, E. J., McMillan, W. W., Warner, J., Streets, D. G., Zhang, Q., Wang, Y., and Wu, S.: Source attribution and interannual variability of Arctic pollution in spring constrained by aircraft (ARCTAS, ARCPAC) and satellite (AIRS) observations of carbon monoxide, *Atmos. Chem. Phys.*, 10, 977–996, doi:10.5194/acp-10-977-2010, 2010.
- Frey, M. M., Hutterli, M. A., Chen, G., Sjøstedt, S. J., Burkhart, J. F., Friel, D. K., and Bales, R. C.: Contrasting atmospheric boundary layer chemistry of methylhydroperoxide (CH₃OOH) and hydrogen peroxide (H₂O₂) above polar snow, *Atmos. Chem. Phys.*, 9, 3261–3276, doi:10.5194/acp-9-3261-2009, 2009.
- Fried, A., Wang, Y., Cantrell, C., Wert, B., Walega, J., Ridley, B., Atlas, E., Shetter, R., Lefer, B., Coffey, M. T., Hannigan, J., Blake, D., Blake, N., Meinardi, s., Talbot, B., Dibb, J., Scheuer, E., Wingenter, O., Snow, J., Heikes, B., and Ehhalt, D.: Tunable diode laser measurements of formaldehyde during the TOPSE 2000 study: Distributions, trends, and model comparisons, *J. Geophys. Res.*, 108, 8365, doi:10.1029/2002JD002208, 2003.
- Fuchs, H., Bohn, B., Hofzumahaus, A., Holland, F., Lu, K. D., Nehr, S., Rohrer, F., and Wahner, A.: Detection of HO₂ by laser-induced fluorescence: calibration and interferences from RO₂ radicals, *Atmos. Meas. Tech.*, 4, 1209–1225, doi:10.5194/amt-4-1209-2011, 2011.
- Fuelberg, H. E., Harrigan, D. L., and Sessions, W.: A meteorological overview of the ARCTAS 2008 mission, *Atmos. Chem. Phys.*, 10, 817–842, doi:10.5194/acp-10-817-2010, 2010.
- Jacob, D. J., Crawford, J. H., Maring, H., Clarke, A. D., Dibb, J. E., Emmons, L. K., Ferrare, R. A., Hostetler, C. A., Russell, P. B., Singh, H. B., Thompson, A. M., Shaw, G. E., McCauley, E., Pederson, J. R., and Fisher, J. A.: The Arctic Research of the Composition of the Troposphere from Aircraft and Satellites (ARCTAS) mission: design, execution, and first results, *Atmos. Chem. Phys.*, 10, 5191–5212, doi:10.5194/acp-10-5191-2010, 2010.
- Kwan, A. J., Crounse, J. D., Clarke, A., Shinozuka, Y., Anderson, B. E., Crawford, J. H., Avery, M. A., McNaughton, C., Brune, W. H., Singh, H. B., and Wennberg, P. O.: On the flux of oxygenated volatile organic compounds from organic aerosol oxidation, *Geophys. Res. Lett.*, 33, L15815, doi:10.1029/2006GL026144, 2006.
- Law, K. S. and Stohl, A.: Arctic air pollution: origins and impacts, *Science*, 315, 1537–1540, doi:10.1126/science.1137695, 2007.

- Lee, M., D. O'Sullivan, Noone, K. B., and Heikes, B. G.: HPLC method for determination of H_2O_2 , C_1 and C_2 hydroperoxides in the atmosphere, *J. Atmos. Oceanic Technol.*, 12, 1060–1070, 1995.
- Lemke, P., Ren, J., Alley, R. B., Allison, I., Carrasco, J., Flato, G., Fujii, Y., Kaser, G., Mote, P., Thomas, R. H., and Zhang, T.: Observations: Changes in Snow, Ice and Frozen Ground, *Climate Change 2007: The Physical Science Basis. Contribution of Working Group I to the Fourth Assessment Report of the Intergovernmental Panel on Climate Change*, edited by: Solomon, S., Qin, D., Manning, M., Chen, Z., Marquis, M., Averyt, K. B., Tignor, M., and Miller, H. L., Cambridge University Press, Cambridge, United Kingdom and New York, NY, USA, 2007.
- Li, S., Matthews, J., and Sinha, A.: Atmospheric Hydroxyl Radical Production from Electronically Excited NO_2 and H_2O , *Science*, 319, 1657–1660, 2008.
- Liao, J., Huey, L. G., Tanner, D. J., Brough, N., Brooks, S., Dibb, J. E., Stutz, J., Thomas, J. L., Lefer, B., Haman, C., and Gorham, K.: Observations of hydroxyl and peroxy radicals and the impact of BrO at Summit, Greenland in 2007 and 2008, *Atmos. Chem. Phys.*, 11, 8577–8591, doi:10.5194/acp-11-8577-2011, 2011.
- Logan, J. A., Prather, M. J., Wofsy, S. C., and McElroy, M. B.: Tropospheric chemistry: A global perspective, *J. Geophys. Res.*, 86, 7210–7254, 1981.
- Lurmann, F. W., Lloyd, A. C., and Atkinson, R.: A chemical mechanism for use in long-range transport/acid deposition computer modeling, *J. Geophys. Res.*, 91, 10905–10936, 1986.
- Madronich, S. and Flocke, S.: The role of solar radiation in atmospheric chemistry, in: *Handbook of Environmental Chemistry*, edited by: Boule, P., 1–26, Springer, New York, 1998.
- Mahajan, A. S., Shaw, M., Oetjen, H., Hornsby, K. E., Carpenter, L. J., Kaleschke, L., Tian-Kunze, X., Lee, J. D., Moller, S. J., Edwards, P., Commane, R., Ingham, T., Heard, D. E., and Plane, J. M.: Evidence of reactive iodine chemistry in the Arctic boundary layer, *J. Geophys. Res.*, 115, D20303, doi:10.1029/2009JD013665, 2010.
- Mao, J., Jacob, D. J., Evans, M. J., Olson, J. R., Ren, X., Brune, W. H., Clair, J. M. St., Crounse, J. D., Spencer, K. M., Beaver, M. R., Wennberg, P. O., Cubison, M. J., Jimenez, J. L., Fried, A., Weibring, P., Walega, J. G., Hall, S. R., Weinheimer, A. J., Cohen, R. C., Chen, G., Crawford, J. H., McNaughton, C., Clarke, A. D., Jaeglé, L., Fisher, J. A., Yantosca, R. M., Le Sager, P., and Carouge, C.: Chemistry of hydrogen oxide radicals (HO_x) in the Arctic troposphere in spring, *Atmos. Chem. Phys.*, 10, 5823–5838, doi:10.5194/acp-10-5823-2010, 2010.
- Mao, J., Ren, X., Brune, W. H., Van Duin, D. M., Cohen, R. C., Park, J.-H., Goldstein, A. H., Paulot, F., Beaver, M. R., Crounse, J. D., Wennberg, P. O., DiGangi, J. P., Henry, S. B., Keutsch, F. N., Park, C., Schade, G. W., Wolfe, G. M., and Thornton, J. A.: Insights into hydroxyl measurements and atmospheric oxidation in a California forest, *Atmos. Chem. Phys. Discuss.*, 12, 6715–6744, doi:10.5194/acpd-12-6715-2012, 2012.
- Mauldin III, R. L., Tanner, D. J., and Eisele, F. L.: Measurements of OH during PEM-Tropics A, *J. Geophys. Res.*, 104, 5817–5827, 1999.
- McElroy, C. T., McLinden, C. A., and McConnell, J. C.: Evidence for bromine monoxide in the free troposphere during the Arctic polar sunrise, *Nature*, 397, 338–341, doi:10.1038/16904, 1999.
- Neuman, J. A., Nowak, J. B., Huey, L. G., Burkholder, J. B., Dibb, J. E., Holloway, J. S., Liao, J., Peischl, J., Roberts, J. M., Ryerson, T. B., Scheuer, E., Stark, H., Stickel, R. E., Tanner, D. J., and Weinheimer, A.: Bromine measurements in ozone depleted air over the Arctic Ocean, *Atmos. Chem. Phys.*, 10, 6503–6514, doi:10.5194/acp-10-6503-2010, 2010.
- Olson, J. R., Crawford, J. H., Chen, G., Brune, W. H., Faloona, I. C., Tan, D., Harder, H., and Martinez, M.: A reevaluation of airborne HO_x observations from NASA field campaigns, *J. Geophys. Res.*, 111 D10301, doi:10.1029/2005JD006617, 2006.
- Oltmans, S. J.: Surface ozone measurements in clean air, *J. Geophys. Res.*, 86, 1174–1180, 1981.
- Oltmans, S. J. and Komhyr, W.: Surface ozone distributions and variations from 1973–1984: measurements at the NOAA geophysical monitoring for climatic change baseline observatories, *J. Geophys. Res.*, 91, 5229–5236, doi:10.1029/JD091iD04p05229, 1986.
- Orlando, J. J. and Tyndall, G. S.: Rate coefficients for the thermal decomposition of BrONO_2 and the heat of formation of BrONO_2 , *J. Phys. Chem.*, 100, 19298–19405, 1996.
- Quinn, P. K., Bates, T. S., Baum, E., Doubleday, N., Fiore, A. M., Flanner, M., Fridlind, A., Garrett, T. J., Koch, D., Menon, S., Shindell, D., Stohl, A., and Warren, S. G.: Short-lived pollutants in the Arctic: their climate impact and possible mitigation strategies, *Atmos. Chem. Phys.*, 8, 1723–1735, doi:10.5194/acp-8-1723-2008, 2008.
- Radke, L., Hobbs, P., and Bailey, I.: Airborne observations of Arctic aerosols. III: Origins and effects of airmasses, *Geophys. Res. Lett.*, 11, 401–404, doi:10.1029/GL011i005p00401, 1984.
- Ren, X., Mao, J., Brune, W. H., Cantrell, C. A., Mauldin III, R. L., Hornbrook, R. S., Kosciuch, E., Olson, J. R., Crawford, J. H., Chen, G., and Singh, H. B.: Airborne intercomparison of HO_x measurements using laser-induced fluorescence and chemical ionization mass spectrometry during ARCTAS, *Atmos. Meas. Tech. Discuss.*, 5, 2529–2565, doi:10.5194/amtd-5-2529-2012, 2012.
- Rinsland, C. P., Coheur, P. F., Herbin, H., Clerbaux, C., Boone, C., Bernath, P., and Chiou, L. S.: Detection of elevated tropospheric hydrogen peroxide (H_2O_2) mixing ratios in atmospheric chemistry experiment (ACE) subtropical infrared solar occultation spectra, *J. Quant. Spectrosc. Ra.*, 107, 340–348, 2007.
- Sachse, G., Hill, G., Wade, L., and Perry, M.: Fast-response, high-precision carbon monoxide sensor using a tunable diode laser absorption technique, *J. Geophys. Res.*, 92, 2095–2081, 2008.
- Saiz-Lopez, A., Plane, J. M. C., Baker, A., Carpenter, L. J., von Glasow, R., Gomez Martin, J. C., McFiggans, G., and Saunders, R. W.: Atmospheric Chemistry of Iodine, *Chem. Rev.*, 112, 1773–1804, doi:10.1021/cr200029u, 2011.
- Sander, S. P., Fridl, R. R., Ravishankara, A. R., Golden, D. M., Kolb, C. E., Kurylo, M. J., Molina, M. J., Moortgat, G. K., Finlayson-Pitts, B. J., Wine, P. H., Huie, R. E., and Orkin, V. L.: Chemical kinetics and photochemical data for use in atmospheric studies, Evaluation Number 15, JPL Publ., 06-2, 2006.
- Scheuer, E., Talbot, R. W., Dibb, J. E., Seid, G. K., deBell, L., and Lefer, G.: Seasonal distributions of fine aerosol sulfate in the North American Arctic Basin during TOPSE, *J. Geophys. Res.*, 108, 8370, doi:10.1029/2001JD001364, 2003.
- Shaw, G. E.: The Arctic phase phenomenon, *B. Am. Meteorol. Soc.*, 76, 2403–2413, 1995.

- Shetter, R. E. and Muller, M.: Photolysis frequency measurements using actinic flux spectroradiometry during the PEM-Tropics mission: Instrumentation description and some results, *J. Geophys. Res.*, 104, 5647–5661, 1999.
- Shindell, D. T., Faluvegi, G., Bauer, S. E., Koch, D. M., Unger, N., Menon, S., Miller, R. L., Schmidt, G. A., and Streets, D. G.: Climate response to projected changes in short-lived species under an A1B scenario from 200–2050 in the GISS climate model, *J. Geophys. Res.*, 112, D20103, doi:10.1029/2007JD008753, 2007.
- Shindell, D. T., Chin, M., Dentener, F., Doherty, R. M., Faluvegi, G., Fiore, A. M., Hess, P., Koch, D. M., MacKenzie, I. A., Sanderson, M. G., Schultz, M. G., Schulz, M., Stevenson, D. S., Teich, H., Textor, C., Wild, O., Bergmann, D. J., Bey, I., Bian, H., Cuvelier, C., Duncan, B. N., Folberth, G., Horowitz, L. W., Jonson, J., Kaminski, J. W., Marmer, E., Park, R., Pringle, K. J., Schroeder, S., Szopa, S., Takemura, T., Zeng, G., Keating, T. J., and Zuber, A.: A multi-model assessment of pollution transport to the Arctic, *Atmos. Chem. Phys.*, 8, 5353–5372, doi:10.5194/acp-8-5353-2008, 2008.
- Singh, H. B., Brune, W. H., Crawford, J. H., Jacob, D. J., and Russell, P. B.: Overview of the summer 2004 Intercontinental Chemical Transport Experiment – North America (INTEX-A), *J. Geophys. Res.*, 111, D24S01, doi:10.1029/2006JD007905, 2006.
- Singh, H. B., Anderson, B. E., Brune, W. H., Cai, C., Cohen, R. C., Crawford, J. H., Cubison, M. J., Czech, E. P., Emmons, L., Fuelberg, H. E., Huey, G., Jacob, D. J., Jimenez, J. L., Kaduwela, A., Kondo, Y., Mao, J., Olson, J. R., Sachse, G. W., Vay, S. A., Weinheimer, A., Wennberg, P. O., Wisthaler, A., and the ARC-TAS Science Team: Pollution influences on atmospheric composition and chemistry at high northern latitudes: Boreal and California forest fire emissions, *Atmos. Environ.*, 44, 4553–4564, doi:10.1016/j.atmosenv.2010.08.026, 2010.
- Slusher, D. L., Huey, L. G., Tanner, D. J., Flocke, F. M., and Roberts, J. M.: A thermal dissociation-chemical ionization mass spectrometry (td-cims) technique for the simultaneous measurement of peroxyacyl nitrates and dinitrogen pentoxide, *J. Geophys. Res.*, 109, D19315, doi:10.1029/2004JD004670, 2004.
- Snow, J. A., Heikes, B. G., Merrill, J. T., Wimmers, A. J., Moody, J. L., and Cantrell, C. A.: Winter-spring evolution and variability of HOx reservoir species, hydrogen peroxide, and methyl hydroperoxide in the northern middle to high latitudes, *J. Geophys. Res.*, 108, 8362, doi:10.1029/2002JD002172, 2003.
- Snow, J. A., Heikes, B. G., Shen, H., O'Sullivan, D. W., Fried, A., and Walega, J.: Hydrogen peroxide, methyl hydroperoxide, and formaldehyde over North America and the North Atlantic, *J. Geophys. Res.*, 112, D12S07, doi:10.1029/2006JD007746, 2007.
- Soller, R., Nicovich, J., and Wine, P.: Temperature-dependent rate coefficients for the reactions of $\text{Br}(\text{}^2\text{P}_{3/2})$, $\text{Cl}(\text{}^2\text{P}_{3/2})$, and $\text{O}(\text{}^3\text{P})$ with BrONO_2 , *J. Phys. Chem. A*, 105, 1416–1422, 2001.
- Stohl, A.: Characteristics of atmospheric transport into the Arctic troposphere, *J. Geophys. Res.*, 111, D11306, doi:10.1029/2005JD006888, 2006.
- Stroud, C., Madronich, S., Atlas, E., Cantrell, C., Fried, A., Wert, B., Ridley, B., Eisele, F., Mauldin, L., Shetter, R., Lefer, B., Flocke, F., Weinheimer, A., Coffey, M., Heikes, B., Talbot, R., and Blake, C.: Photochemistry in the Arctic free troposphere: Ozone budget and its dependence on nitrogen oxides and the production rate of free radicals, *J. Atmos. Chem.*, 47, 107–138, 2004.
- Thornton, J. A., Jaeglé, L., and McNeill, V. F.: Assessing known pathways for HO_2 loss in aqueous atmospheric aerosols: Regional and global impacts on tropospheric oxidants, *J. Geophys. Res.*, 113, D05303, doi:10.1029/2007jd009236, 2008.
- von Glasow, R., von Kuhlmann, R., Lawrence, M. G., Platt, U., and Crutzen, P. J.: Impact of reactive bromine chemistry in the troposphere, *Atmos. Chem. Phys.*, 4, 2481–2497, doi:10.5194/acp-4-2481-2004, 2004.
- Weibring, P., Richter, D., Walega, J. G., and Fried, A.: First demonstration of a high performance difference frequency spectrometer on airborne platforms, *Optics Express*, 15, 13476–13495, 2007.
- Weinheimer, A. J., Walega, J. G., Ridley, B. A., Gary, G. L., Blake, D. R., Blake, N. J., Rowland, F. S., Sachse, G. W., Anderson, B. E., and Collins, J. E.: Meridional distributions of NO_x , NO_y and other species in the lower stratosphere and upper troposphere during AASE II, *Geophys. Res. Lett.*, 21, 2583–2586, 1994.
- Wisthaler, A., Hansel, A., Dickerson, R. R., and Crutzen, P. J.: Organic trace gas measurements by PTR-MS during INDOEX 1999, *J. Geophys. Res.*, 107, 8024, doi:10.1029/2001JD000576, 2002.